INTERNATIONAL JOURNAL FOR NUMERICAL METHODS IN FLUIDS
*Int. J. Numer. Meth. Fluids* 2008; **57**:715–744
Published online 25 October 2007 in Wiley InterScience (www.interscience.wiley.com). DOI: 10.1002/fld.1639

# Time-accurate stabilized finite-element model for weakly nonlinear and weakly dispersive water waves

Zhengyong Zhong and K. H. Wang*, †

*Department of Civil and Environmental Engineering, University of Houston, Houston, TX 77204-4003, U.S.A.*

## SUMMARY

Introduction of a time-accurate stabilized finite-element approximation for the numerical investigation of weakly nonlinear and weakly dispersive water waves is presented in this paper. To make the time approximation match the order of accuracy of the spatial representation of the linear triangular elements by the Galerkin finite-element method, the fourth-order time integration of implicit multistage Padé method is used for the development of the numerical scheme. The streamline-upwind Petrov–Galerkin (SUPG) method with crosswind diffusion is employed to stabilize the scheme and suppress the spurious oscillations, usually common in the numerical computation of convection-dominated flow problems. The performance of numerical stabilization and accuracy is addressed. Treatments of various boundary conditions, including the open boundary conditions, the perfect reflecting boundary conditions along boundaries with irregular geometry, are also described. Numerical results showing the comparisons with analytical solutions, experimental measurements, and other published numerical results are presented and discussed. Copyright © 2007 John Wiley & Sons, Ltd.

Received 19 September 2006; Revised 3 September 2007; Accepted 6 September 2007

KEY WORDS: Boussinesq equations; solitary wave; implicit multistage Padé method; streamline-upwind Petrov–Galerkin; crosswind diffusion

## INTRODUCTION

Boussinesq equations are commonly used to describe weakly nonlinear and weakly dispersive water waves in a variable depth environment. The original system of Boussinesq equations was proposed by Peregine [1]. In the past two decades, many researchers, Madsen *et al.* [2], Nwogu [3], and Wu [4], among others, have also derived improved Boussinesq systems in an effort to extend their application.

*Correspondence to: K. H. Wang, Department of Civil and Environmental Engineering, University of Houston, Houston, TX 77204-4003, U.S.A.
†E-mail: khwang@uh.edu

Meanwhile, numerical study of those Boussinesq systems has also been an active research subject. Most of the numerical Boussinesq models, Abbott *et al.* [5], Nwogu [3], Wei and Kirby [6], and others, are based on finite-difference methods using rectangular grids. In order to deal with geometric complexity, a boundary-fitted coordinate system was also introduced into Boussinesq modeling by Wang *et al.* [7], Li and Zhan [8], and Shi *et al.* [9]. The finite-difference method is simple to use and the best for regular geometric areas; however, for more complicated domains, local mesh refinements are usually preferred in regions with rapidly varying boundaries or depth. Even when non-uniform grids are used, it is still relatively hard for standard rectangular grids or structured curvilinear grids to achieve such grid adjustment. Instead, unstructured finite-element grids are well qualified for fitting the irregular domains. In the last decade, significant advances have been made in Boussinesq modeling using finite-element method. Katopodes and Wu [10] and Antunes do Carmo *et al.* [11] pioneered probably the earliest finite-element Boussinesq models but they were limited to the original Boussinesq equations and structured grids. Kawahara and Cheng [12] have applied linear finite-element method to the equations using fully unstructured meshes. Many other researchers have focused on solving the improved Boussinesq systems by finite-element method introducing different auxiliary variables for the second- or higher-order spatial derivatives appearing in the equations. The Boussinesq model given by Wu [13] was solved by Langtangen and Pederson [14] with bi-quadratic finite elements. Li *et al.* [15] developed a linear quadrilateral finite-element model for the extended Boussinesq equations due to Beji and Nadaoka [16]. More recently, Walkley and Berzins [17, 18] investigated both one- and two-dimensional finite-element methods using Nwogu's [3] extended Boussinesq equations. Woo and Liu [19] published a finite-element model using Nwogu's [3] equations too, and then applied it to study the nonlinear harbor oscillation problems. For their own extended Boussinesq equations [2], Sørensen *et al.* [20] proposed a finite-element method in which mixed interpolations (linear and quadratic) and mixed elements (triangular and quadrilateral) were applied to stabilize the spurious modes.

Among those finite-element Boussinesq models, many have reported the occurrence of spurious modes especially when linear unstructured finite elements were used for the spatial discretization, but not much effort has been made to solve the problem. Spurious oscillations are very common in finite-element modeling of all kinds of flow problems. When the convection effect dominates, as the case for the propagation of shallow-water waves described by Boussinesq equations, the high-frequency oscillations may adversely affect the numerical results. According to the analysis of Donea and Huerta [21], the non-physical oscillations in the Galerkin finite-element method for convective problems arise from its second-order centered difference nature with a negative numerical diffusion truncation error inherent in the scheme. The irregularity of unstructured computational grids may also lead to the lower order truncation errors as a result of the variation of mesh size over the domain and irregular connection pattern of meshes, which accordingly could generate negative impact on the accuracy of the numerical solutions. On the other hand, if the computational mesh is structured with uniform size or even the mesh pattern somehow follows the flow pattern, there could be some cancelation of truncation errors. In order to stabilize the convective term, among many other stabilization techniques, the streamline-upwind Petrov–Galerkin (SUPG) method proposed by Hughes and Mallet [22] has gained great success. The basic idea of the SUPG method is to introduce an additional diffusion term to the weighting function to counteract the negative dissipation introduced by the Galerkin formulation. The SUPG method is a linear high-order method and consequently some oscillations will remain in regions containing sharp layers, un-resolvable on the finite-element meshes. As a remedy, Hughes and Mallet [23] added a nonlinear diffusion term (discontinuity capturing term) along the direction of the gradient vector of



DOI: 10.1002/fld

the unknowns. However, as pointed out by Codina [24], this term modifies the streamline diffusion and may introduce negative numerical diffusion. Thus, he suggested to keep unaltered diffusion in the direction of the streamlines and to introduce crosswind diffusion terms to improve the stability of the numerical solutions.

Interactions of solitary waves with a solid vertical cylinder or cylinder arrays have been investigated for many years. Isaacson [25] was among the pioneers to derive analytical solutions using a Fourier integral transform for a first approximation. Yates and Wang [26] reported an experimental study of solitary waves scattered by a vertical cylinder. Experimental data were presented for the wave elevations and the forces on the vertical circular cylinder. Using the finite-difference method, Wang *et al.* [7] and Wang and Jiang [27] carried out numerical analyses of solitary waves interacting with a vertical cylinder and cylinder arrays. In the framework of the finite-element method, this problem was also tested by Ambrosi and Quartapelle [28] and Woo and Liu [19].

In this paper, the SUPG finite-element method with crosswind diffusion is applied to solve the Boussinesq equations. This is coupled with the highly accurate implicit multistage Padé method for time integration, as proposed by Donea and Huerta [29]. This model is demonstrated to be able to obtain accurate oscillation-free results using simple linear triangular elements. Simulated results for head-on collision of solitary waves are presented. In addition, the model is applied to investigate the scattering of a solitary wave by a vertical cylinder. The results are compared with experimental measurements and other numerical solutions. Extension of the model is also carried out to simulate a solitary wave propagating over a semicircular shoal, which introduces the effect of variable depth, to further illustrate the performance of the present finite-element Boussinesq model.

## GOVERNING EQUATIONS

Under the assumptions of incompressible, inviscid fluid, and irrotational motion of water, the three-dimensional nonlinear waves evolving and propagating in two horizontal dimensions on shallow water with variable depth may be represented by the following Boussinesq equations derived by Peregrine [1] and Wu [13]:

$$\frac{\partial \zeta^*}{\partial t^*} + \nabla^* \cdot [(h^* + \zeta^*)\mathbf{u}^*] = 0 \tag{1}$$

$$\frac{\partial \mathbf{u}^*}{\partial t^*} + \frac{h^{*2}}{6}\nabla^*\left(\nabla^* \cdot \frac{\partial \mathbf{u}^*}{\partial t^*}\right) - \frac{h^*}{2}\nabla^*\left[\nabla^* \cdot \left(h^* \frac{\partial \mathbf{u}^*}{\partial t^*}\right)\right] + \mathbf{u}^* \cdot \nabla^* \mathbf{u}^* + g\nabla^* \zeta^* = 0 \tag{2}$$

where $z^* = \zeta^*(x^*, y^*, t^*)$ is the free-surface elevation as measured from the still water level; $\mathbf{u}^* = (u^*, v^*)$ is the depth-averaged velocity of the three-dimensional velocity $\mathbf{v}^*(x^*, y^*, z^*, t^*)$; $h^*(x^*, y^*)$ is the still water depth, and $g$ is the gravitational acceleration. Throughout this paper, a variable in bold indicates a vector. The superscript $*$ denotes dimensional variables and $\nabla^* = (\partial/\partial x^*, \partial/\partial y^*)$ is the horizontal gradient operator in Cartesian coordinates.

For the convenience of presenting and examining the numerical results, we rewrite Equations (1) and (2) in terms of dimensionless variables defined as $\mathbf{u} = \mathbf{u}^*/\sqrt{gh_0^*}$, $(x, y, \zeta, h) =$



DOI: 10.1002/fld

$(x^*, y^*, \zeta^*, h^*)/h_0^*$, and $t=\sqrt{gh_0^*}t^*/h_0^*$, where $h_0^*$ is a reference water depth. Equations (1) and (2) in dimensionless form then read

$$\zeta_t+\nabla\cdot[(h+\zeta)\mathbf{u}]=0 \tag{3}$$

$$\mathbf{u}_t+\frac{h^2}{6}\nabla(\nabla\cdot\mathbf{u}_t)-\frac{h}{2}\nabla[\nabla\cdot(h\mathbf{u}_t)]+(\mathbf{u}\cdot\nabla)\mathbf{u}+\nabla\zeta=0 \tag{4}$$

where the subscript $t$ denotes differentiation in time. Introducing the multidimensional spatial differential operator $L$ and the auxiliary vector variable $\mathbf{w}$ as

$$\mathbf{w}=(w_x, w_y)=L\mathbf{u}=-\frac{h^2}{6}\nabla(\nabla\cdot\mathbf{u})+\frac{h}{2}\nabla[\nabla\cdot(h\mathbf{u})] \tag{5}$$

Equation (4) can be simplified to

$$(1-L)\mathbf{u}_t+(\mathbf{u}\cdot\nabla)\mathbf{u}+\nabla\zeta=0 \tag{6}$$

Furthermore, we rearrange the terms in Equations (3) and (4) to obtain the expressions of time derivatives of the basic unknowns, namely,

$$\zeta_t=-\nabla\cdot[(h+\zeta)\mathbf{u}] \tag{7}$$

$$\mathbf{u}_t=(1-L)^{-1}[-(\mathbf{u}\cdot\nabla)\mathbf{u}-\nabla\zeta] \tag{8}$$

The above equations are used for the temporal and spatial discretizations.

## NUMERICAL SCHEME

To conveniently apply the stabilization techniques to the unsteady nonlinear problems, it is preferable that the time discretization be performed before the spatial discretization. Therefore, the time integration scheme of our finite-element Boussinesq model is discussed first.

### *Time integration scheme*

As remarked by Donea [30], using the conventional Galerkin finite-element approach in the solution of convection problems, the discretization based on uniform mesh of piecewise linear elements yields a fourth-order spatial accuracy , while the central finite-difference method is only second-order accurate in the spatial derivatives. Moreover, in the numerical approximation of convection or convection-dominated problems, space and time are linked by the characteristics and the discretization of one certainly influences the other. Proper coupling between the time discretization and the Galerkin spatial approximation of hyperbolic problems is thus needed. $C^0$-continuous finite elements can approximate only up to second-order spatial derivatives with the application of Green's theorem. If the governing equations have terms up to second-order spatial derivatives, time integration algorithms are limited to involve only first-order time derivatives when they are combined with $C^0$-continuous finite-element approximations. To meet this requirement and achieve the same order of temporal approximation as the spatial approximation given by the Galerkin method, Donea and Huerta [29] proposed a high-order time-stepping method—the fourth-order implicit multistage Padé scheme emanating from the factorization of Padé approximations



DOI: 10.1002/fld

to the exponential function. Adopting this scheme to march the numerical solution from a given time $t^n = n\Delta t$ to the next time level $t^{n+1} = t^n + \Delta t$, the time integration scheme involving only first-order time derivatives and two implicit time stages, for Boussinesq equations, reads

$$\zeta^{n+1/2} - \zeta^n = \frac{\Delta t}{24}(5\zeta_t^n + 8\zeta_t^{n+1/2} - \zeta_t^{n+1}) \tag{9a}$$

$$\zeta^{n+1} - \zeta^{n+1/2} = \frac{\Delta t}{24}(-\zeta_t^n + 8\zeta_t^{n+1/2} + 5\zeta_t^{n+1}) \tag{9b}$$

$$\mathbf{u}^{n+1/2} - \mathbf{u}^n = \frac{\Delta t}{24}(5\mathbf{u}_t^n + 8\mathbf{u}_t^{n+1/2} - \mathbf{u}_t^{n+1}) \tag{9c}$$

$$\mathbf{u}^{n+1} - \mathbf{u}^{n+1/2} = \frac{\Delta t}{24}(-\mathbf{u}_t^n + 8\mathbf{u}_t^{n+1/2} + 5\mathbf{u}_t^{n+1}) \tag{9d}$$

where the superscript denotes the time level and $\Delta t$ is the time step.

To introduce the local finite-element residue of each unknown at different time stages, we substitute the time derivatives of the unknowns (Equations (7) and (8)) into the Equations (9a)–(9d) and rearrange them to form the following residual equations:

$$R(\zeta^{n+1/2}) = \zeta^{n+1/2} - \zeta^n + \frac{\Delta t}{24}(5\nabla\cdot[(h+\zeta)\mathbf{u}]^n + 8\nabla\cdot[(h+\zeta)\mathbf{u}]^{n+1/2} - \nabla\cdot[(h+\zeta)\mathbf{u}]^{n+1}) \tag{10a}$$

$$R(\zeta^{n+1}) = \zeta^{n+1} - \zeta^{n+1/2} + \frac{\Delta t}{24}(-\nabla\cdot[(h+\zeta)\mathbf{u}]^n + 8\nabla\cdot[(h+\zeta)\mathbf{u}]^{n+1/2} + 5\nabla\cdot[(h+\zeta)\mathbf{u}]^{n+1}) \tag{10b}$$

$$\begin{aligned} R(\mathbf{u}^{n+1/2}) = (1-L)(\mathbf{u}^{n+1/2} - \mathbf{u}^n) + \frac{\Delta t}{24}(5[(\mathbf{u}\cdot\nabla)\mathbf{u} + \nabla\zeta]^n + 8[(\mathbf{u}\cdot\nabla)\mathbf{u} + \nabla\zeta]^{n+1/2} \\ -[(\mathbf{u}\cdot\nabla)\mathbf{u} + \nabla\zeta]^{n+1}) \end{aligned} \tag{10c}$$

$$\begin{aligned} R(\mathbf{u}^{n+1}) = (1-L)(\mathbf{u}^{n+1} - \mathbf{u}^{n+1/2}) + \frac{\Delta t}{24}(-[(\mathbf{u}\cdot\nabla)\mathbf{u} + \nabla\zeta]^n + 8[(\mathbf{u}\cdot\nabla)\mathbf{u} + \nabla\zeta]^{n+1/2} \\ +5[(\mathbf{u}\cdot\nabla)\mathbf{u} + \nabla\zeta]^{n+1}) \end{aligned} \tag{10d}$$

The remaining spatial discretizations of Equations (10a)–(10d) are addressed in the next subsection.

*SUPG method with crosswind diffusion*

It is well known that the standard Galerkin method has the difficulty of eliminating spurious oscillations when applied to convection-dominated flow problems. Modeling nonlinear water waves as we study herein is a highly convection-dominated problem. Therefore, it becomes necessary to seek effective ways to stabilize the scheme. The SUPG stabilization technique was identified to be a well developed and robust method. It possesses the quality of good stability and accuracy. At the same time, the SUPG method can prevent spurious oscillations from spreading all over the computational domain.



DOI: 10.1002/fld

Subdividing the computational domain into a grid system with linear triangular elements, the dependent variables in Equations (3) and (4) are approximated within an element $\Omega^e$ as follows:

$$f^e \approx \sum_{i=1}^{3} N_i f_i^e \tag{11}$$

where the $f_i^e$ are the values of any dependent variable at the nodal points of the element and $N_i$ are the linear shape functions.

The derivation of finite-element equation for the unknown $\zeta^{n+1/2}$, using the least-squares method, is given below to show the procedure of derivation of finite-element equations for other variables. The integral of the square of the residual $R(\zeta^{n+1/2})$ over an element is required to vanish. This means the derivative of the integral with respect to each nodal value of $\zeta_k^{n+1/2}$ must be zero. After substituting $\zeta^{n+1/2}$ with the expression of Equation (11) into Equation (10a), the above-described minimizing condition leads to

$$\frac{\partial \int\int_{\Omega^e} R^2(\zeta^{n+1/2})\,\mathrm{d}x\,\mathrm{d}y}{\partial \zeta_k^{n+1/2}} = 2\int\int_{\Omega^e}\left(N_k + \frac{\Delta t}{3}\nabla\cdot(N_k\mathbf{u}^{n+1/2})\right)R(\zeta^{n+1/2})\,\mathrm{d}x\,\mathrm{d}y = 0 \tag{12a}$$

or

$$\int\int_{\Omega^e} N_k R(\zeta^{n+1/2})\,\mathrm{d}x\,\mathrm{d}y + \int\int_{\Omega^e}\frac{1}{3}\tau^{n+1/2}\nabla\cdot(N_k\mathbf{u}^{n+1/2})R(\zeta^{n+1/2})\,\mathrm{d}x\,\mathrm{d}y = 0 \tag{12b}$$

It can be seen from Equation (12a) or (12b), in addition to the standard weighting function $N_k$, another weighting term, $(\tau^{n+1/2}/3)\nabla\cdot(N_k\mathbf{u}^{n+1/2})$, has been rigorously derived in establishing the element equation for $\zeta^{n+1/2}$. This term adds the effect of streamline diffusion for the removal of non-physical oscillations along the streamline direction. With the addition of the streamline diffusion term, the finite-element formulation developed here is similar to the Galerkin/least-squares method as referred by Hughes *et al.* [31]. Here, the time step $\Delta t$ in the second weighting term has been replaced by $\tau^{n+1/2}$ to have some control of the amount of the added diffusion. $\tau$ is the stabilization parameter, intrinsic time, which varies with time step, grid size, and the velocity magnitude. Following the idea of Shakib [32], for different time stage it is defined as

$$(\tau^e)^{n+1/2} = \frac{\dfrac{1}{3}}{\sqrt{\left(\dfrac{1}{\Delta t}\right)^2 + \left(\dfrac{1}{3}\dfrac{2\|\overline{\mathbf{u}}^e\|^{n+1/2}}{\delta l^e}\right)^2}} \tag{13a}$$

$$(\tau^e)^{n+1} = \frac{\dfrac{5}{24}}{\sqrt{\left(\dfrac{1}{\Delta t}\right)^2 + \left(\dfrac{5}{24}\dfrac{2\|\overline{\mathbf{u}}^e\|^{n+1}}{\delta l^e}\right)^2}} \tag{13b}$$



DOI: 10.1002/fld

where $l^e$ is a length scale representing the element size, $\delta$ is a constant, and $\|\overline{\mathbf{u}}^e\|$ is the norm of element-averaged velocity vector, defined as

$$\overline{\mathbf{u}}^e = \frac{1}{A^e}\int\int_{\Omega^e} \mathbf{u}\,\mathrm{d}x\,\mathrm{d}y = \frac{1}{A^e}\int\int_{\Omega^e} (N_i u_i \mathbf{i} + N_i v_i \mathbf{j})\,\mathrm{d}x\,\mathrm{d}y$$
$$= \frac{1}{3}(u_1+u_2+u_3)\mathbf{i} + \frac{1}{3}(v_1+v_2+v_3)\mathbf{j} \tag{14}$$

Here, $A^e$ is the element area and $(u_i, v_i)$, $i=1,2,3$, represent the velocity components at the nodal points of an element. In this study, the diameter of the inscribed circle of a triangular element is used for $l^e$.

To remove the oscillations remaining due to the absence of control of the solution gradient in directions other than along the streamlines, a crosswind diffusion term is proposed to be included in Equation (12b). Then, we have

$$\int\int_{\Omega^e} N_k R(\zeta^{n+1/2})\,\mathrm{d}x\,\mathrm{d}y + \int\int_{\Omega^e} \frac{1}{3}\tau^{n+1/2}\nabla\cdot(N_k\mathbf{u}^{n+1/2})R(\zeta^{n+1/2})\,\mathrm{d}x\,\mathrm{d}y$$
$$+\int\int_{\Omega^e} \frac{1}{3}\upsilon_{\zeta^{n+1/2}}\nabla N_{k\perp}\cdot\nabla\zeta_\perp^{n+1/2}\,\mathrm{d}x\,\mathrm{d}y = 0 \tag{15}$$

where $\nabla\zeta_\perp^{n+1/2}$ denotes the crosswind derivative of $\zeta^{n+1/2}$ and $\upsilon_{\zeta^{n+1/2}}$ is the crosswind viscosity for $\zeta^{n+1/2}$. For the expression of $\nabla\zeta_\perp^{n+1/2}$, let us assume $f$ to be any dependent variable, we have

$$\nabla f_\perp = P_\perp\cdot\nabla f \tag{16}$$

where the tensorial structure $P_\perp = \mathbf{I} - \mathbf{u}\otimes\mathbf{u}/\|\mathbf{u}\|^2$ , $\mathbf{I}$, being the unit tensor, is the orthogonal projector onto the crosswind direction, and $\otimes$ denotes the tensorial product between two vectors. According to Codina [24], the nonlinear crosswind viscosity $\upsilon_f$ can be expressed as

$$\upsilon_f = \begin{cases} \frac{1}{2}\delta l^e |R^e(f)|/\|\overline{\nabla f^e}\| & \text{if } \|\overline{\nabla f^e}\|\neq 0 \\ 0 & \text{otherwise} \end{cases} \tag{17}$$

where $R^e(f) = (1/A^e)\int\int_{\Omega^e} R(f)\,\mathrm{d}x\,\mathrm{d}y$, $\overline{\nabla f^e} = (1/A^e)\int\int_{\Omega^e}\nabla f\,\mathrm{d}x\,\mathrm{d}y$, and $R(f)$'s are given in (10a)–(10d). Detailed expressions of $R^e(f)$ and $\overline{\nabla f^e}$ for all dependent variables can be found in Zhong [33].

Following a similar procedure, the finite-element equations for $\zeta^{n+1}$, $u^{n+1/2}$, $u^{n+1}$, $v^{n+1/2}$, and $v^{n+1}$ with the addition of crosswind diffusion terms can be written as

$$\int\int_{\Omega^e} W_k R(\zeta^{n+1})\,\mathrm{d}x\,\mathrm{d}y + \int\int_{\Omega^e} \frac{5}{24}\tau^{n+1}\nabla\cdot(W_k\mathbf{u}^{n+1})R(\zeta^{n+1})\,\mathrm{d}x\,\mathrm{d}y$$
$$+\int\int_{\Omega^e} \frac{5}{24}\upsilon_{\zeta^{n+1}}\nabla W_{k\perp}\cdot\nabla\zeta_\perp^{n+1}\,\mathrm{d}x\,\mathrm{d}y = 0 \tag{18a}$$



DOI: 10.1002/fld

$$\int\int_{\Omega^e} W_k R(u^{n+1/2})\,\mathrm{d}x\,\mathrm{d}y+\int\int_{\Omega^e}\frac{1}{3}\tau^{n+1/2}\nabla W_k\cdot\mathbf{u}^{n+1/2}R(u^{n+1/2})\,\mathrm{d}x\,\mathrm{d}y$$

$$+\int\int_{\Omega^e}\frac{1}{3}\upsilon_{u^{n+1/2}}\nabla W_{k\perp}\cdot\nabla u_{\perp}^{n+1/2}\,\mathrm{d}x\,\mathrm{d}y=0 \tag{18b}$$

$$\int\int_{\Omega^e} W_k R(u^{n+1})\,\mathrm{d}x\,\mathrm{d}y+\int\int_{\Omega^e}\frac{5}{24}\tau^{n+1}\nabla W_k\cdot\mathbf{u}^{n+1}R(u^{n+1})\,\mathrm{d}x\,\mathrm{d}y$$

$$+\int\int_{\Omega^e}\frac{5}{24}\upsilon_{u^{n+1}}\nabla W_{k\perp}\cdot\nabla u_{\perp}^{n+1}\,\mathrm{d}x\,\mathrm{d}y=0 \tag{18c}$$

$$\int\int_{\Omega^e} W_k R(v^{n+1/2})\,\mathrm{d}x\,\mathrm{d}y+\int\int_{\Omega^e}\frac{1}{3}\tau^{n+1/2}\nabla W_k\cdot\mathbf{u}^{n+1/2}R(v^{n+1/2})\,\mathrm{d}x\,\mathrm{d}y$$

$$+\int\int_{\Omega^e}\frac{1}{3}\upsilon_{v^{n+1/2}}\nabla W_{k\perp}\cdot\nabla v_{\perp}^{n+1/2}\,\mathrm{d}x\,\mathrm{d}y=0 \tag{18d}$$

$$\int\int_{\Omega^e} W_k R(v^{n+1})\,\mathrm{d}x\,\mathrm{d}y+\int\int_{\Omega^e}\frac{5}{24}\tau^{n+1}\nabla W_k\cdot\mathbf{u}^{n+1}R(v^{n+1})\,\mathrm{d}x\,\mathrm{d}y$$

$$+\int\int_{\Omega^e}\frac{5}{24}\upsilon_{v^{n+1}}\nabla W_{k\perp}\cdot\nabla v_{\perp}^{n+1}\,\mathrm{d}x\,\mathrm{d}y=0 \tag{18e}$$

where $W_k$ is the weighting function and, here, is identical to the shape function $N_k$ of the element.

Applying Green's theorem to the weighted element integral of the auxiliary vector variable $\mathbf{w}$ in Equation (5), we have

$$\int\int_{\Omega^e} W_k\mathbf{w}\,\mathrm{d}x\,\mathrm{d}y=\int\int_{\Omega^e} W_k L\mathbf{u}\,\mathrm{d}x\,\mathrm{d}y=\int\int_{\Omega^e} W_k\left\{\frac{h^2}{3}\nabla(\nabla\cdot\mathbf{u})+\frac{h}{2}[\nabla\cdot\mathbf{u}\nabla h+\nabla(\nabla h\cdot\mathbf{u})]\right\}\mathrm{d}x\,\mathrm{d}y$$

$$=\frac{1}{2}\int\int_{\Omega^e} W_k h\nabla\cdot\mathbf{u}\nabla h\,\mathrm{d}x\,\mathrm{d}y-\frac{1}{3}\int\int_{\Omega^e}\nabla(W_k h^2)(\nabla\cdot\mathbf{u})\,\mathrm{d}x\,\mathrm{d}y-\frac{1}{2}\int\int_{\Omega^e}\nabla(W_k h)(\nabla h\cdot\mathbf{u})\,\mathrm{d}x\,\mathrm{d}y$$

$$+\frac{1}{3}\int_{\Gamma^e} W_k h^2(\nabla\cdot\mathbf{u})\mathbf{n}\,\mathrm{d}s+\frac{1}{2}\int_{\Gamma^e} W_k h(\nabla h\cdot\mathbf{u})\mathbf{n}\,\mathrm{d}s \tag{19}$$

For the inner domain nodes, the line integrals in the expression will cancel out each other. At the wall boundary nodes, only the tangential component of $\mathbf{w}$ in Equation (19) is needed for solving the tangential momentum equations. Therefore, the line integrals are omitted in the computation. As a result, the spatial discretization is applied only to the area integrals in Equation (19).

Substituting Equations (10a)–(10d) with the use of Equation (11) for each unknown variable into Equations (15), (18a)–(18e), and (19) and performing element integrations, we can construct



DOI: 10.1002/fld

a series of spatially discretized element equations of the variables, which are assembled at each nodal point to formulate the final algebraic equations. Expressions of the spatial discretization of each term shown in Equations (15), (18a)–(18e), and (19) are summarized in Appendix A. Solving this system of equations by a standard successive over-relaxation iterative method, the unknowns at each node can be determined for a given time level.

## INITIAL AND BOUNDARY CONDITIONS

For the cases investigated in this paper, Equations (3) and (4) for $\zeta$ and $\mathbf{u}$ are to be solved with appropriate initial and boundary conditions over the flow domain and boundaries. A solitary wave profile with dimensionless amplitude $\alpha$ situated initially at $x=x_0$ is considered as the incident wave condition. Here, $\alpha=a^*/h_0^*$ and $a^*$ is a dimensional wave amplitude. The selection of initial solitary wave solutions for the modeling study is critically important. A set of second-order closed-form solutions derived by Schember [34] for a solitary wave in a domain of constant depth has been adopted for solitary wave modeling study by Wang *et al.* [7]. However, Schember's [34] solitary wave solutions are not the exact solutions of Equations (3) and (4). As noted in many numerical studies of Boussinesq equations [6, 17], if an approximate solution of the governing equations is specified as the initial condition, a slightly higher amplitude solitary wave is formed together with a phase lag and a small dispersive tail trailing behind the main wave crest, compared with the approximate analytical solution.

To produce more accurate numerical solutions, it is preferable to have exact solutions as the initial conditions of the differential governing equations. The procedure of deriving a permanent wave form solution satisfying exactly Equations (3) and (4) (when $h=1$) has been addressed by Teng and Wu [35]. For a right-going solitary wave, the inputted incident wave elevation and depth-averaged horizontal velocity for the present study are obtained by solving the following equations for $\zeta$ and $U$:

$$\zeta=\frac{U}{1-U} \tag{20}$$

$$(U_X)^2=(3-U)U^2-\frac{(U_0-3)U_0^2}{U_0+\ln(1-U_0)}[U+\ln(1-U)] \tag{21}$$

where $U=u/c$, $X=x-ct-x_0$, $U(0)=U_0$, and both $u$ and $\zeta$ are functions of $X$. $c=c^*/\sqrt{gh_0^*}$ is a constant dimensionless phase speed to be determined as

$$c=\pm\sqrt{6\frac{U_0+\ln(1-U_0)}{(U_0-3)U_0^2}} \tag{22a}$$

or

$$c=\pm\sqrt{\frac{6(1+\alpha)^2}{\alpha^2(2\alpha+3)}[(1+\alpha)\ln(1+\alpha)-\alpha]} \tag{22b}$$

As Equations (20) and (21) give the exact solitary wave solutions for the initial condition, the boundary condition for solid walls also needs to be applied. Following Engelman *et al.* [36], we consider a locally rotated coordinate system—$(\overline{n}, T)$ at a wall boundary node in which $\overline{n}$ is aligned



DOI: 10.1002/fld

with the outward normal and $T$ is the tangent. The outward normal vector $\overline{\mathbf{n}}=(\overline{n}_x, \overline{n}_y)$ and the tangent vector $\mathbf{T}=(T_x, T_y)$ are the basis vectors corresponding to $\overline{n}$ and $T$-axis. At a reflective wall boundary, the condition of impermeability requires that the normal velocity is equal to zero, i.e.

$$u_{\overline{n}}=0 \tag{23}$$

At a wall boundary node, since the normal velocity is specified, only the momentum equation in the tangential direction is solved for the tangential velocity $u_T$. The tangential element momentum equation is obtained from the inner product of the element equation of the velocity vectors (Equations (18b)–(18e)) in the Cartesian coordinate system with the tangential vector $\mathbf{T}$ at that boundary node. Finally, the $x$ and $y$-components of the velocity vector at the node are recovered from the following relations:

$$u=T_x u_T - T_y u_{\overline{n}}=T_x u_T \tag{24a}$$

$$v=T_y u_T + T_x u_{\overline{n}}=T_y u_T \tag{24b}$$

Along the right or left open boundary, the radiation condition is applied to propagate waves out of the computational domain. Here, we adopt the linear radiation condition as an approximation of the open boundary conditions in dimensionless form

$$\mathbf{u}_t \pm \mathbf{u}_x = 0 \tag{25a}$$

$$\zeta_t \pm \zeta_x = 0 \tag{25b}$$

where '+' is for the right open boundary, '−' is for the left open boundary. These open boundary conditions have been proved to be able to effectively propagate waves out of the computational domain with negligible artificial reflection [7]. Following a similar discretization technique as described above, the finite-element equations of Equations (25a) and (25b) are solved using the fourth-order time integration of implicit multiple stage Padé method and the SUPG method with crosswind diffusion at open boundaries.

## RESULTS

### *Tests of the performance of numerical model and initial wave conditions*

The newly developed finite-element Boussinesq model described in the previous sections is first validated by comparing results with analytical and other numerical solutions for the case of plane solitary waves propagating through a rectangular channel with a constant depth. The $z$-axis points upward, with the plane $z=0$ at the level of undisturbed water surface. The dimensions of the channel and the initial wave amplitude are $0\leqslant x\leqslant 60$, $0\leqslant y\leqslant 6$, and $\alpha=0.5$, where $x$ denotes the wave propagation direction and $y$ is the transverse direction. Both $x$ and $y$ are made non-dimensional using the undisturbed water depth $h_0^*$. Unstructured triangular elements of an average size of $l^e=0.2$, $\Delta t=0.2$ and the constant $\delta=2.0$ are used in the numerical computations. For the purpose of comparison, the three-dimensional perspective view plots showing part of the free-surface



DOI: 10.1002/fld

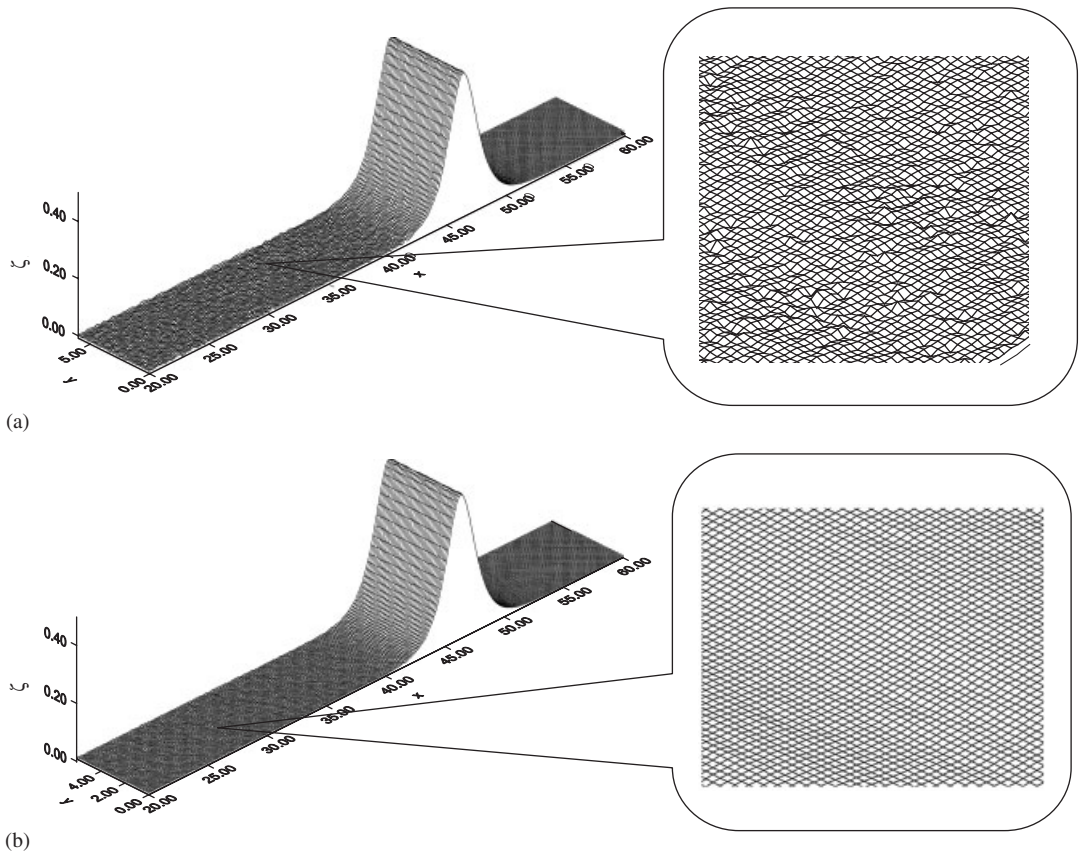


Figure 1. Comparisons of free-surface elevations at $t=30$ ($\alpha=0.5$): (a) finite-element method without stabilization and (b) present model with stabilization.

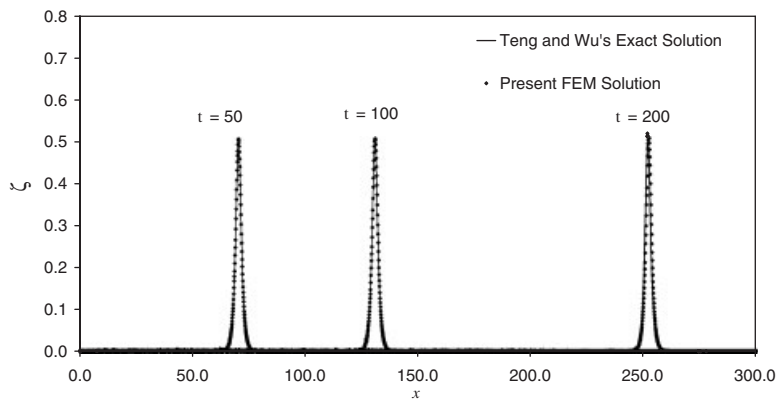


Figure 2. Comparisons of solitary wave profiles obtained from the present FE model and Teng and Wu's [35] exact solution for a long simulation time with $\alpha=0.5$.



DOI: 10.1002/fld

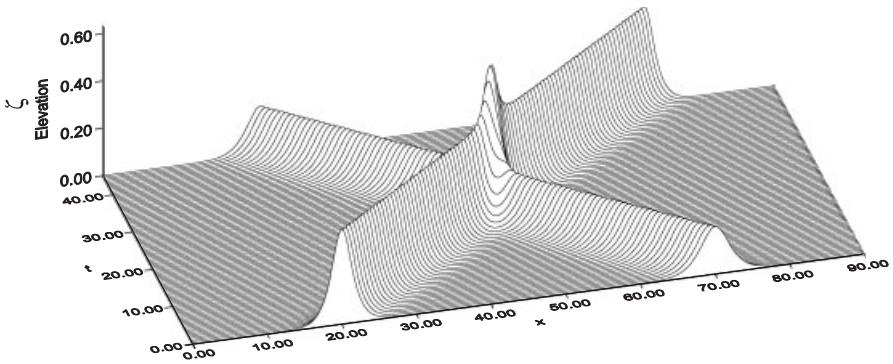


Figure 3. Perspective view plot of wave elevations along the centerline of the computational domain at different instants showing head-on collision of two solitary waves with dimensionless amplitudes of 0.4 and 0.2.

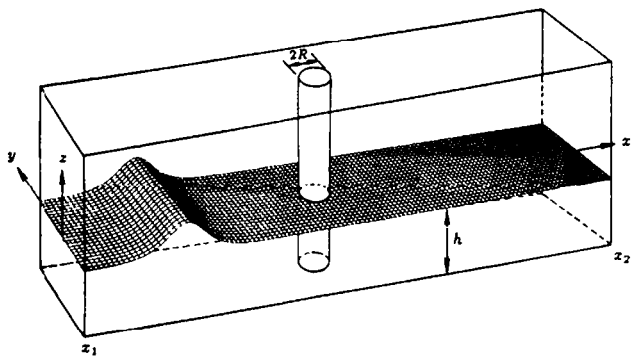


Figure 4. Schematic diagram of initial solitary waves incident upon a surface-piercing vertical cylinder.

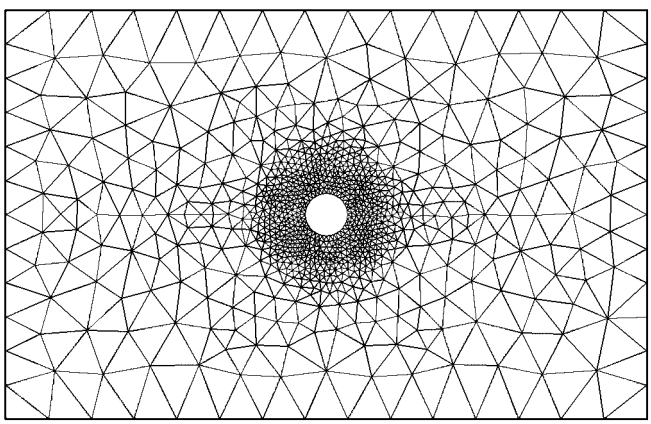

Figure 5. Example plot showing unstructured triangular meshes for modeling solitary waves interaction with a vertical cylinder.



DOI: 10.1002/fld

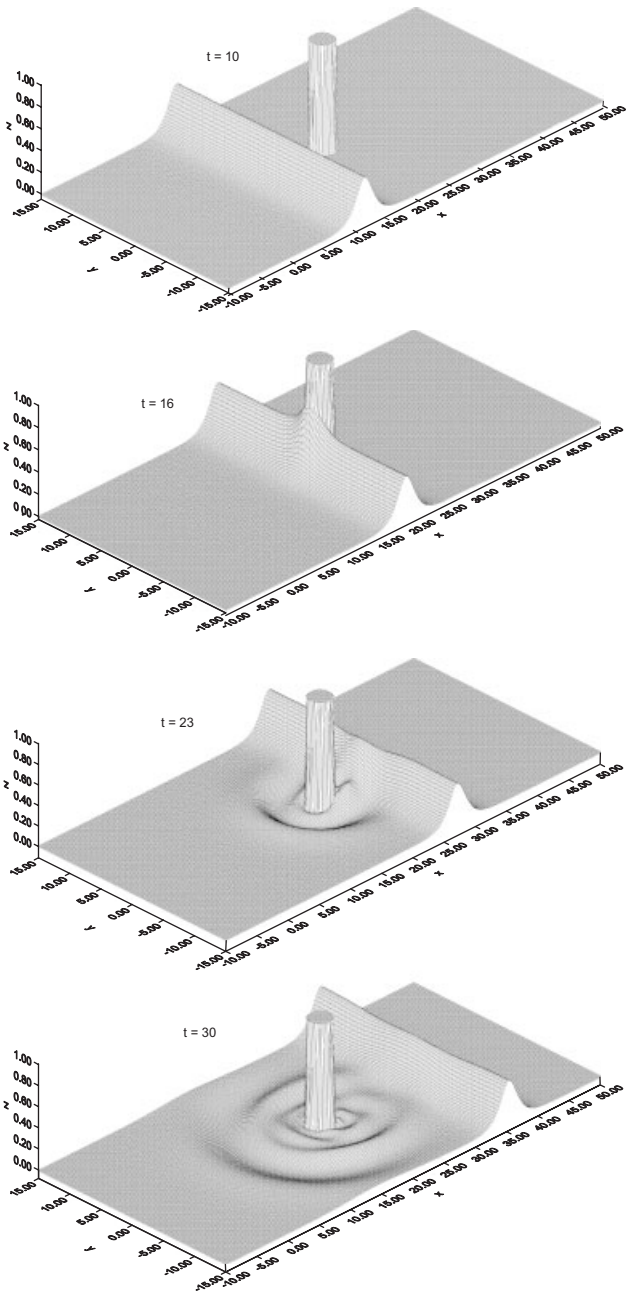


Figure 6. Three-dimensional time-sequence perspective view plot of free-surface elevation for $\alpha = 0.4$.



DOI: 10.1002/fld

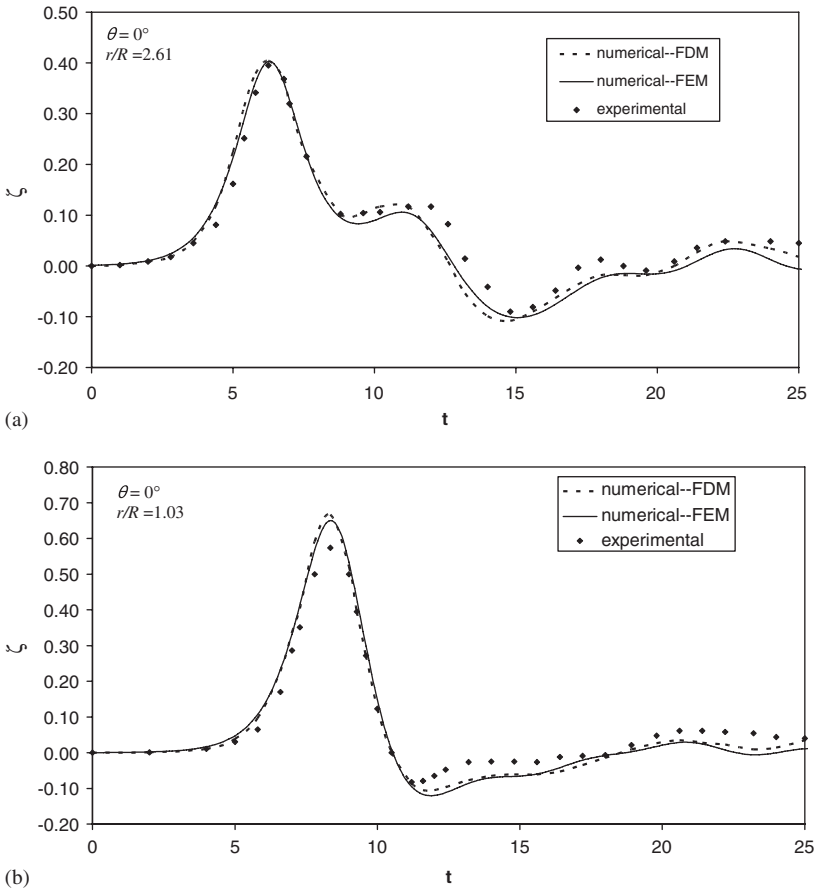


Figure 7. Free-surface elevation $\zeta$ as a function of time along $\theta=0°$ at (a) $r/R=2.61$ and (b) $r/R=1.03$ (—- present model, - - - - [7], ♦♦♦ [26]).

elevation at $t=30$ after traveling from an initial position $x=10.0$ are presented in Figure 1. Here, $t$ is non-dimensionalized using $\sqrt{h_0^*/g}$. Figure 1(a) depicts the results by the finite-element method without stabilization and Figure 1(b) shows the free-surface elevation at the same instant computed using the present model with the implementation of the stabilization technique. Clearly, the wave surface is very smooth and the shape of the wave has been well maintained when the proposed stabilization technique is used; otherwise, the spurious oscillations as shown in Figure 1(a) would appear in the flow domain.

To demonstrate the performance of the present Boussinesq model for a long simulation time and examine the exact representation of the initial solitary wave condition, model is simulated for a free wave traveling in a domain with dimensionless length extended to 300 using the initial wave conditions from Equations (20) and (21). Presented in Figure 2 are the simulated free-surface profiles along the central line of the channel at different instants and the exact solitary wave solutions of Equations (20) and (21). It is found that the solutions of present model agree well with the Teng and Wu's [35] exact solitary wave solutions in terms of wave amplitude and phase speed. After a long simulation time ($t=200$), the amplitude of the solitary wave still maintains



DOI: 10.1002/fld

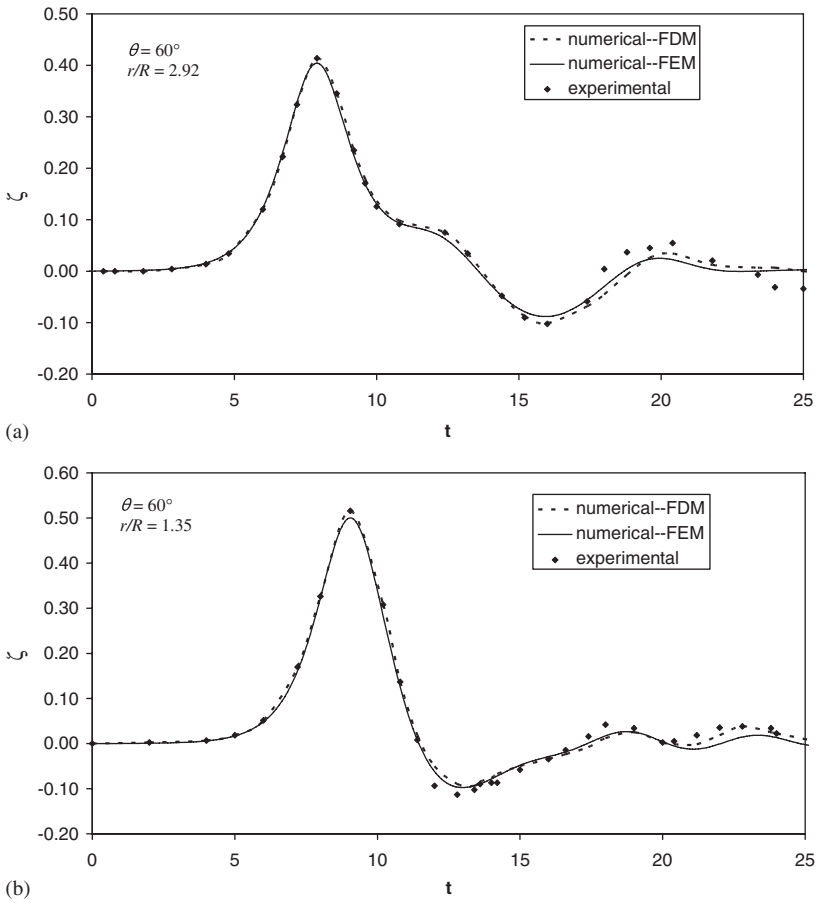


Figure 8. Free-surface elevation $\zeta$ as a function of time along $\theta = 60°$ at (a) $r/R = 2.92$ and (b) $r/R = 1.35$ (—- present model, - - - - [7], ♦♦♦ [26]).

nearly the same as the initial amplitude of 0.5. The numerical solutions of the present model do not show any dispersive tails behind the primary waves as observed by other researchers [6, 17] using the approximate initial wave condition. Figure 2 also indicates that the numerically predicted phase speed matches very well with the exact solution for a long simulation time.

*Modeling head-on collision of two solitary waves*

Head-on collision of two solitary waves is a classical problem that has been studied analytically [37–39] and numerically [40, 41]. It is also a widely used case to test the performance of nonlinear shallow-water wave models. The physical process of wave propagation and associated wave–wave interaction can be examined. In this study, two solitary waves with dimensionless wave amplitudes of 0.4 and 0.2 propagating in opposite direction are inputted for simulation. The solitary wave with amplitude of 0.4 is assumed to propagate along the positive $x$ direction, whereas the 0.2-amplitude solitary wave propagates along the negative $x$ direction.



DOI: 10.1002/fld

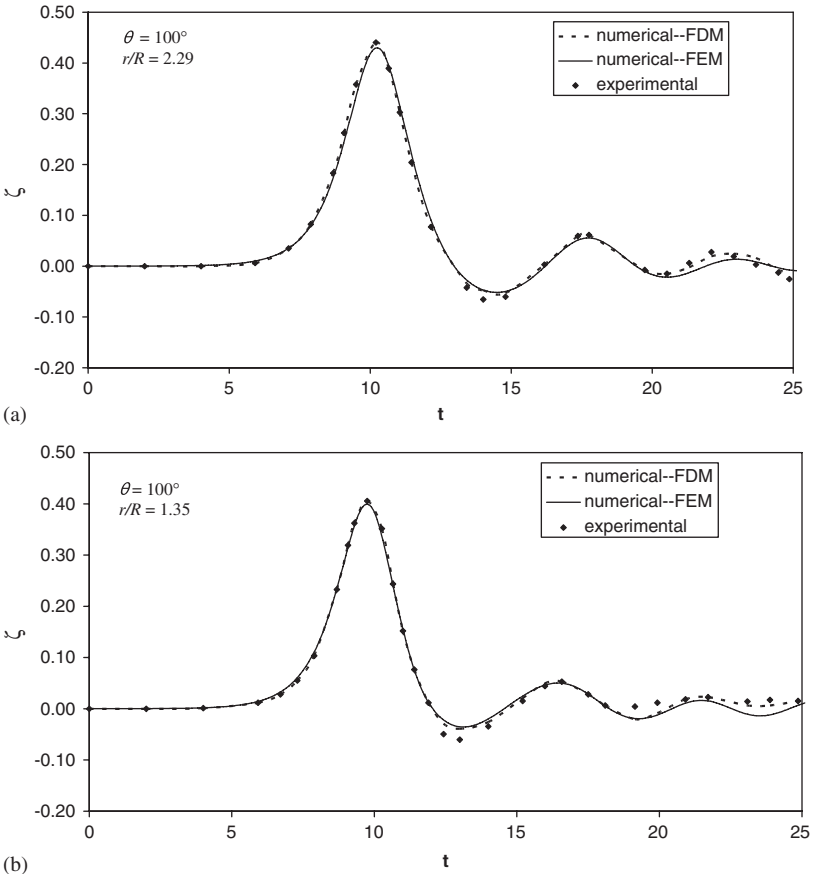


Figure 9. Free-surface elevation $\zeta$ as a function of time along $\theta = 100°$ at (a) $r/R = 2.29$ and (b) $r/R = 1.35$ (—- present model, - - - - [7], ♦♦♦ [26]).

The head-on collision simulation is performed in a two-dimensional domain of narrow channel. The perspective view plot of wave elevations along the centerline of the spatial domain at different instants is shown in Figure 3. The evolution of two solitary waves before, during, and after the interaction can be clearly observed. Two solitary waves meet together to form a single solitary wave with amplitude reaching 0.642 at the stage of maximum interaction ($t = 22.2$), which agrees well with the analytical results reported in Su and Mirie [38], i.e. $\alpha_1 + \alpha_2 + \frac{1}{2}\alpha_1\alpha_2 = 0.64$. It can be seen that each individual wave emerges to recover its original wave form and continue the path of movement in its respective propagating direction. However, during the process of interaction of nonlinear waves, the exchange and transformation of energy causes a slightly delayed wave separation and results in a phase shift for waves before and after the collision. Similar to other studies' findings, the height of the peak during the collision is shown to be slightly greater than the sum of the two wave amplitudes. It is found that the present finite-element Boussinesq model produces similar results to those presented in Li *et al.* [41].



DOI: 10.1002/fld

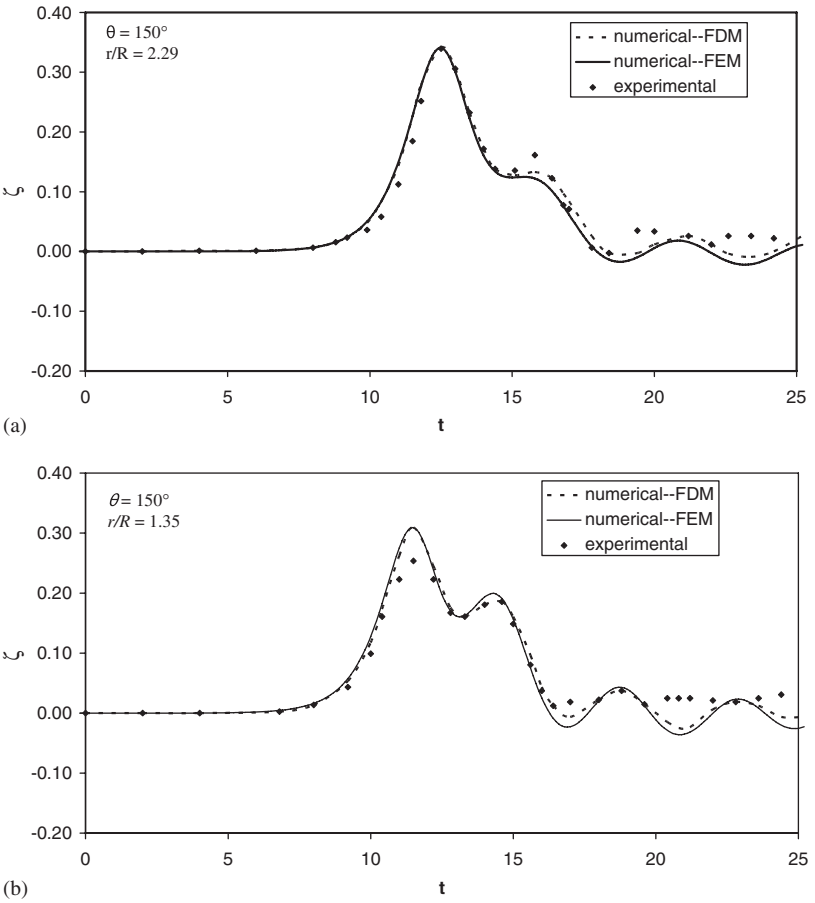


Figure 10. Free-surface elevation $\zeta$ as a function of time along $\theta = 150°$ at (a) $r/R = 2.29$ and (b) $r/R = 1.35$ (—- present model, - - - - [7], ♦♦♦ [26]).

*Modeling a solitary wave interaction with a vertical cylinder*

To show the performance of the present developed model for simulating three-dimensional wave propagation and wave–structure interaction, we use it to study the scattering of a solitary wave by a vertical surface-piercing circular cylinder, as shown in the definition sketch in Figure 4. The dimensions of the computational domain in a channel of constant water depth are $-10 \leqslant x \leqslant 50$ and $-15 \leqslant y \leqslant 15$. The cylinder with dimensionless radius $R = 1.5875$ is fixed in the center of the channel at $(20, 0)$. The radius of the cylinder is selected to be the same as the one used in Yates and Wang's [26] experimental study so that comparisons can be made between model results and measured data. Again, the domain is subdivided into a mesh of unstructured triangular elements of an average size of $l^e = 0.2$; but local refinement in the region surrounding the cylinder has been applied so that smaller elements are distributed around the cylinder. An example plot showing the unstructured coarse grid system is illustrated in Figure 5. A more refined grid system with an average size of $l^e = 0.2$ was used to produce results for solitary waves interacting with a vertical



DOI: 10.1002/fld

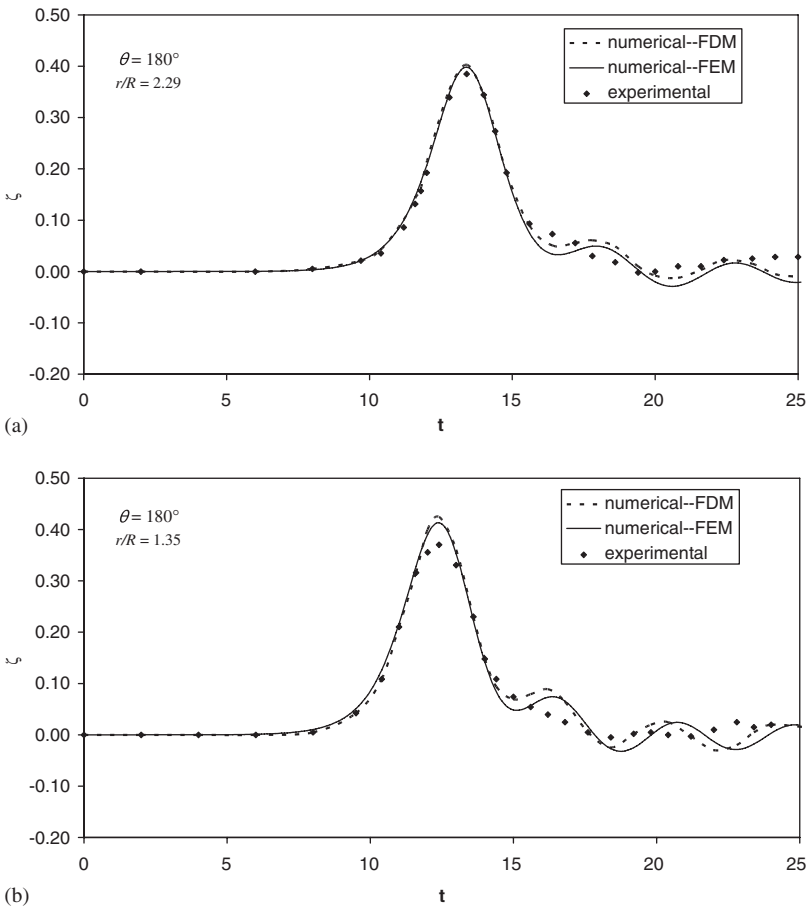


Figure 11. Free-surface elevation $\zeta$ as a function of time along $\theta = 180°$ at (a) $r/R = 2.29$ and (b) $r/R = 1.35$ (—- present model, - - - - [7], ♦♦♦ [26]).

cylinder. For regions away from the cylinder, the grid size is about 0.2, while near the cylinder the grid size is as small as 0.05. The time step $\Delta t = 0.1$ and the constant $\delta$ used in Equations (13a), (13b), and (17) is taken to be 2.0. At the beginning, a plane solitary wave is placed between the left boundary and the cylinder with sufficient distance from the cylinder to have still water level around the cylinder. The wave then is allowed to travel in two horizontal dimensions towards the cylinder. Figure 6 shows a time sequence of three-dimensional perspective view plots of the free-surface elevation for $\alpha = 0.4$. At $t = 10$, the incident solitary wave is approaching the cylinder. When the wave peak impacts on the cylinder, the solitary wave simply piles up in front of the cylinder surface at $t = 16$. Once the primary wave propagates past the cylinder ($t = 23$), the diffraction of local waves around the cylinder is already evident; while the central part of the primary wave has a lower height but does not suffer from any phase lag with respect to the rest of the wave. After the wave has traveled a distance of more than 15 water depths beyond the cylinder, at $t = 30$, a sequence of significant scattered waves propagating away from the cylinder can be observed; however, the



DOI: 10.1002/fld

variation of amplitude of the primary wave remains as the impinging solitary wave tends to recover its initial shape. These features have also been noticed by other authors (for example, [7, 28]). Regarding the maximum run-up at the cylinder, the present model predicts a value of 0.656 at $t=15.8$. For comparison, with an initial wave amplitude of $\alpha=0.3$, the present model provides a prediction of 0.5, which is close to the 0.47 obtained by Ambrosi and Quartapelle [28].

For the case of a solitary wave interaction with a vertical cylinder, comparisons between the present finite-element solutions and the experimental measurements of wave elevation at selected locations around the cylinder [26] are presented in Figures 7–11. Results from the finite-difference Boussinesq model of [7] are also plotted for comparison. The dimensionless incident wave amplitude is 0.4. Figures 7–11 show the time variation of the wave elevations along the upstream centerline ($\theta=0°$) and other angular directions ($\theta=60, 100, 150$, and $180°$).

In Figure 7(a) ($r/R=2.61$ and $\theta=0°$), the main incident wave and a reflected wave followed by a negative wave, which develops into a train of oscillatory waves can be observed. At a location closer to cylinder ($r/R=1.03$), the main wave shows the trend of piling up in front of the cylinder with a maximum amplitude of about 0.65, which is immediately followed by a negative wave, where the first reflected wave already propagates radially outward (Figure 7(b)). A similar wave scattering pattern along $\theta=60°$ line can be noticed from results in Figure 8. From Figures 7 and 8, it appears that the present numerical results show quite good agreement with the experimental measurements. The results from the finite-element model also agree very well with those from the finite-difference model. The numerically predicted maximum amplitude of the main wave at a location very close to the cylindrical surface is slightly greater than the measured one.

On the rear side of the cylinder, wave elevations along the $\theta=100, 150$, and $180°$ (Figures 9–11) show the propagation of the main wave followed by a back-scattered wave and subsequently a train of small oscillatory waves. Good agreement between the predicted wave elevations and measured ones along the angular direction of $100°$ can be noticed. At $\theta=150°$, the amplitude of the main wave near the cylinder (at $r/R=1.35$) is reduced as a result of the blockage by the cylinder. However, the main wave recovers very quickly to its original wave amplitude as shown in Figure 11(b) for wave elevation at $r/R=1.35$ and $\theta=180°$. Again, the present model results show good agreement with experimental measurements and with those from the finite-difference model even at regions behind the cylinder (Figures 9–11). Certainly, the numerical model tends to slightly over-predict the wave amplitude for waves in the region behind and close to the cylinder. The difference in the maximum amplitude may be caused by the viscous effect and flow separation, which are not accounted for in the Boussinesq equations.

*Propagation of a solitary wave over a semicircular shoal*

The present finite-element Boussinesq model is also extended to simulate a solitary wave propagating over a semicircular shoal, which introduces the effect of variable depth. In dimensionless variables, the domain is $(x, y)\in[-15, 60]\times[0, 6.67]$ with $x=-15$ and 60 being the inflow and outflow boundaries, and $y=0$ and 6.67 as the wall boundaries, respectively. The dimensionless water depth within the domain follows the expression given by

$$h(x,y)=\begin{cases}1.0, & -15.0\leqslant x\leqslant 11.67-G\\ 1.0+\dfrac{1}{11.43}(11.67-G-x), & 11.67-G\leqslant x\leqslant 20.0-G\\ 0.271, & 20.0-G\leqslant x\leqslant 60.0\end{cases} \tag{26}$$



DOI: 10.1002/fld

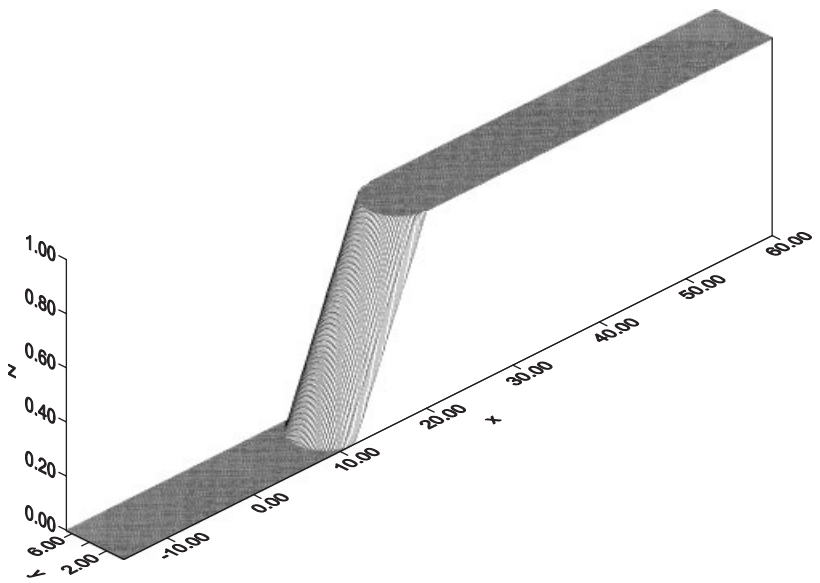


Figure 12. Bottom topography of a semicircular shoal.

where

$$G(y)=[y(6.67-y)]^{1/2}, \quad 0\leqslant y\leqslant 6.67 \tag{27}$$

A perspective view plot of bottom topography of the domain is shown in Figure 12. From Equation (26), it can be noticed that the undisturbed water depth varies from 1 to 0.271 in the shallower water depth region.

The domain is divided into 54 066 triangular elements with an average element size of 0.2. The time step $\Delta t$ is 0.1. At the beginning, a solitary wave of dimensionless amplitude 0.08 is situated at $x=0$. Figure 13 illustrates the propagation and transformation procedure of a solitary wave over the semicircular shoal with a time series of three-dimensional perspective view plots of wave elevation profiles. It is shown clearly from Figure 13 that the wave form has been strongly affected by the bottom curving shoal. At $t=25$, the primary wave crest is gradually amplified at the central region due to wave focusing. A convex wave crestline is formed with a set down of wave elevation occurring right behind the primary wave peak in the middle of the channel. However, the focusing waves, although having higher amplitude, remain propagating at the same pace as the waves along the side walls. Meanwhile, small amplitude waves reflected by the submerged shoal are scattered backward to the left open boundary. Upon entering the region of shallower water depth, the wave energy of the leading wave is redistributed along the crestline, causing the non-uniform wave profile to slosh back and forth across the channel as indicated from plots at $t=25$, 30, and 40. With the waves traveling farther downstream in the shallower water depth area, the interesting wave fission phenomenon showing the appearance of three secondary wave crests with decreasing wave amplitude propagating behind the main incident wave can be observed at $t=70$. The sloshing effect is also noticed to become smaller and smaller. The results present interesting phenomena of wave focusing and the coherent structure of wave propagation due to the well-balanced interplay of both nonlinear and dispersive effects.



DOI: 10.1002/fld

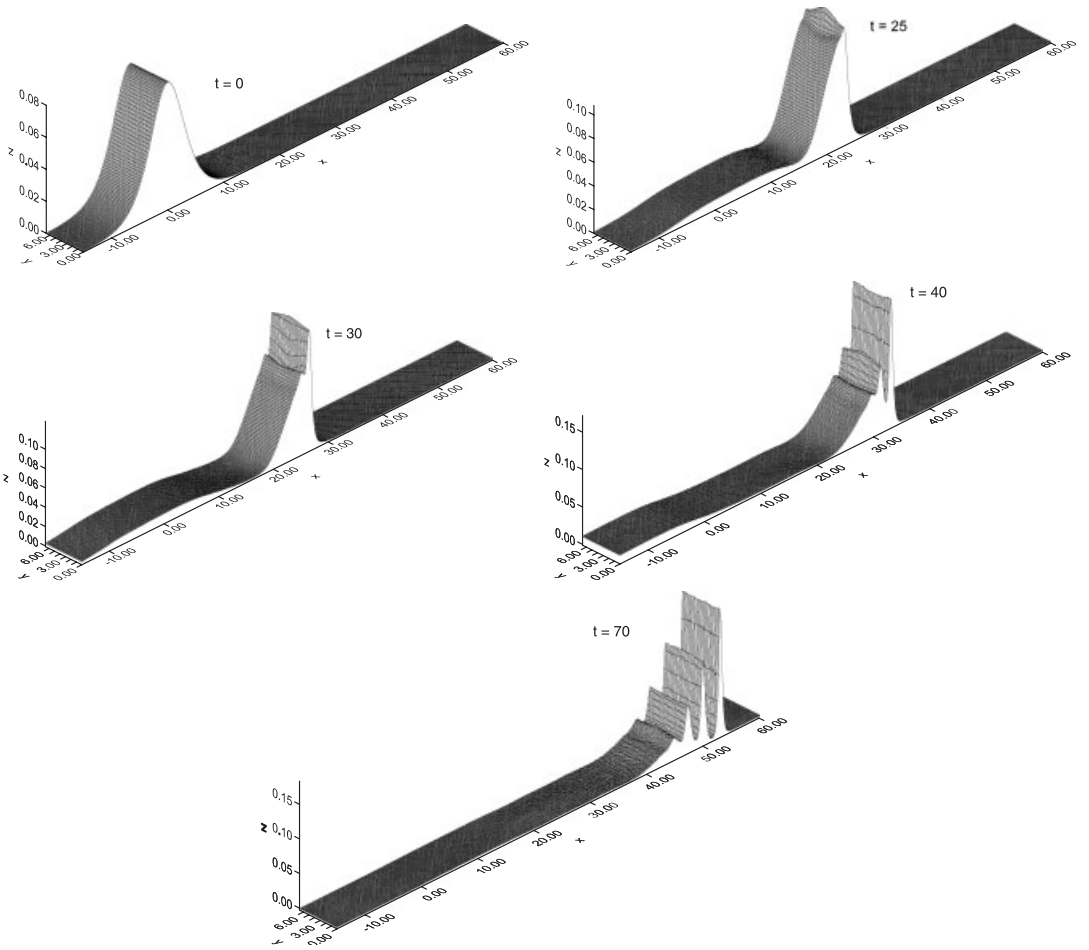


Figure 13. A time sequence of three-dimensional perspective view plots of a solitary wave propagating over a submerged semicircular shoal.

The free-surface elevations are also plotted along the centerline of the channel at various times (Figure 14). After the main wave enters into the region of variable water depth (the submerged shoal region), the peak of the wave begins to tilt forward. At the same time, the reflected waves from the submerged shoal emerge behind the main wave ($t = 20$). However, as soon as the main wave passes the shoal and propagates into the shallower water depth area the whole fission process of transforming the main wave into four separate waves of decreasing wave amplitude is demonstrated clearly in the plots from $t = 30$ to 70. The maximum wave amplitude of the primary wave reached in the shallower water depth region is 0.186. This indicates that the ratio between the wave amplitude and the shallower water depth is about 0.69, which is close to the limitation of the applicable range of weakly nonlinear and weakly dispersive Boussinesq equations.

Overall, the present developed finite-element Boussinesq model can provide stable and accurate predictions on the propagation of nonlinear shallow-water waves in two horizontal dimensions and their interactions with cylindrical structures. The successful modeling of a solitary wave



DOI: 10.1002/fld

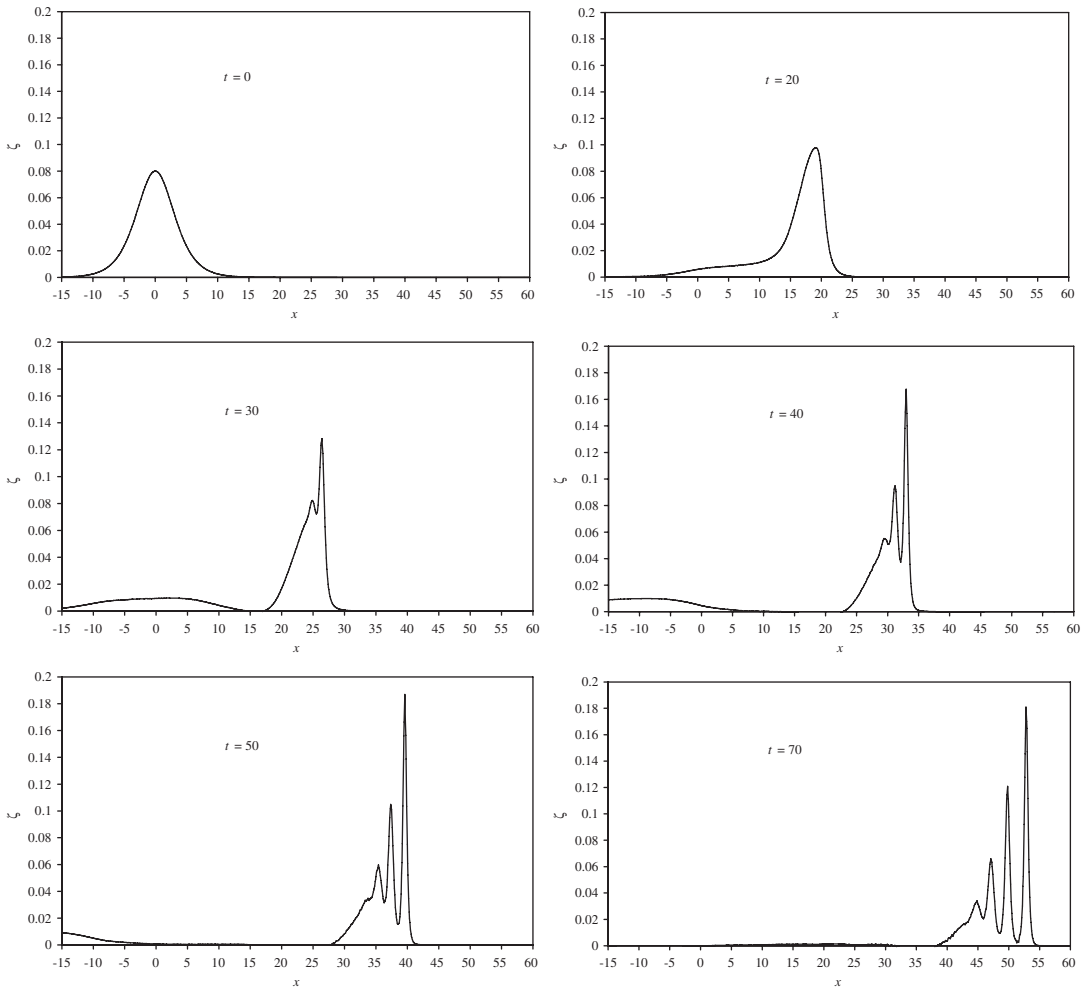


Figure 14. A time sequence of free-surface profiles along the centerline of the channel for a solitary wave propagating over a submerged semicircular shoal.

propagating over a submerged three-dimensional shoal demonstrates again the robustness of the new numerical scheme.

## CONCLUSIONS

A new SUPG finite-element model with crosswind diffusion for the Boussinesq equations is presented in this paper. When properly coupled with the highly accurate implicit multistage Padé time integration scheme, the stabilization technique employed in this model has been proved to be very effective in suppressing spurious oscillations. For the case of a solitary wave propagating at a constant depth, good agreements, in terms of both free-surface amplitude and phase speed,



DOI: 10.1002/fld

are found between present numerical results and analytical solutions, even for a long simulation time. Accurate results are also obtained for modeling head-on collision of two solitary waves. The application of the proposed model to the case of solitary waves propagating past a vertical cylinder reveals two interesting features: Once the primary wave has past the cylinder, the central part of the primary wave has a lower height but does not suffer from any phase lag with respect to the rest of the wave. Moreover, as the incident wave moves farther and farther away from the obstacle, a sequence of significant scattered waves propagate outwards from the cylinder; however, the impinging solitary wave tends to recover its initial shape. The effect of variable depth is also tested from a simulation of a solitary wave propagating past a submerged semi-circular shoal. Interesting wave fission phenomenon showing the appearance of a series of secondary wave crests with decreasing wave amplitude propagating behind the main incident wave can be observed. Model simulations for the results presented in the paper were run in PCs with either single processor or dual processors system. The results can be obtained within a few days to weeks depending on the size of the computational domain and simulation time of interest. The present numerical model is demonstrated to be able to produce relatively accurate and stabilized results, which have shown fairly good agreements with the experimental measurements and other published analytical and numerical solutions.

## APPENDIX A: FINITE ELEMENT FORMULATIONS IN EQUATIONS (15), (18a)–(18e), AND (19)

$$\begin{aligned}\int\int_{\Omega^e} W_k R(\zeta^{n+1/2})\,\mathrm{d}x\,\mathrm{d}y &= M_{ki}\zeta_i^{n+1/2} - M_{ki}\zeta_i^n + \frac{\Delta t}{24}(S_{kij}+O_{kij})[5u_j^n(h_i+\zeta_i^n)\\ &\quad + 8u_j^{n+1/2}(h_i+\zeta_i^{n+1/2}) - u_j^{n+1}(h_i+\zeta_i^{n+1})]\\ &\quad + \frac{\Delta t}{24}(T_{kij}+P_{kij})[5v_j^n(h_i+\zeta_i^n)\\ &\quad + 8v_j^{n+1/2}(h_i+\zeta_i^{n+1/2}) - v_j^{n+1}(h_i+\zeta_i^{n+1})] \end{aligned} \tag{A1}$$

$$\begin{aligned}&\int\int_{\Omega^e} \frac{1}{3}\tau^{n+1/2}\nabla\cdot(W_k\mathbf{u}^{n+1/2})R(\zeta^{n+1/2})\,\mathrm{d}x\,\mathrm{d}y\\ &= \frac{1}{3}\tau^{n+1/2}((O_{kij}+U_{kij})u_j^{n+1/2}+(P_{kij}+V_{kij})v_j^{n+1/2})\zeta_i^{n+1/2}\\ &\quad -\frac{1}{3}\tau^{n+1/2}((O_{kij}+U_{kij})u_j^{n+1/2}+(P_{kij}+V_{kij})v_j^{n+1/2})\zeta_i^{n}\\ &\quad +\frac{5\Delta t}{72}\tau^{n+1/2}\left(\begin{array}{l}((C_{kijl}+Q_{kijl})u_l^{n+1/2}+(E_{kijl}+S_{kijl})v_l^{n+1/2})[u_j^n(h_i+\zeta_i^n)+u_i^n(h_j+\zeta_j^n)]\\ \quad +((D_{kijl}+R_{kijl})u_l^{n+1/2}+(F_{kijl}+T_{kijl})v_l^{n+1/2})[v_j^n(h_i+\zeta_i^n)+v_i^n(h_i+\zeta_j^n)]\end{array}\right)\\ &\quad +\frac{\Delta t}{9}\tau^{n+1/2}\left(\begin{array}{l}((C_{kijl}+Q_{kijl})u_l^{n+1/2}+(E_{kijl}+S_{kijl})v_l^{n+1/2})[u_j^{n+1/2}(h_i+\zeta_i^{n+1/2})+u_i^{n+1/2}(h_i+\zeta_j^{n+1/2})]\\ \quad +((D_{kijl}+R_{kijl})u_l^{n+1/2}+(F_{kijl}+T_{kijl})v_l^{n+1/2})[v_j^{n+1/2}(h_i+\zeta_i^{n+1/2})+v_i^{n+1/2}(h_i+\zeta_j^{n+1/2})]\end{array}\right)\\ &\quad -\frac{\Delta t}{72}\tau^{n+1/2}\left(\begin{array}{l}((C_{kijl}+Q_{kijl})u_l^{n+1/2}+(E_{kijl}+S_{kijl})v_l^{n+1/2})[u_j^{n+1}(h_i+\zeta_i^{n+1})+u_i^{n+1}(h_i+\zeta_j^{n+1})]\\ \quad +((D_{kijl}+R_{kijl})u_l^{n+1/2}+(F_{kijl}+T_{kijl})v_l^{n+1/2})[v_j^{n+1}(h_i+\zeta_i^{n+1})+v_i^{n+1}(h_i+\zeta_j^{n+1})]\end{array}\right)\end{aligned} \tag{A2}$$



DOI: 10.1002/fld

$$\int\int_{\Omega^e} \frac{1}{3} v_{\zeta^{n+1/2}} \nabla W_{k\perp} \cdot \nabla \zeta_{\perp}^{n+1/2} \,\mathrm{d}x\,\mathrm{d}y$$

$$= \frac{1}{3} v_{\zeta^{n+1/2}} \left( J_{ki} + K_{ki} - \frac{1}{\|\mathbf{u}\|^2} ((Q_{kijl} u_l^{n+1/2} + R_{kijl} v_l^{n+1/2}) u_j^{n+1/2} \right.$$

$$\left. + (S_{kijl} u_l^{n+1/2} + T_{kijl} v_l^{n+1/2}) v_j^{n+1/2}) \right) \zeta_i^{n+1/2} \tag{A3}$$

$$\int\int_{\Omega^e} W_k R(\zeta^{n+1}) \,\mathrm{d}x\,\mathrm{d}y$$

$$= M_{ki} \zeta_i^{n+1} - M_{ki} \zeta_i^{n+1/2} + \frac{\Delta t}{24} (S_{kij} + O_{kij}) [-u_j^n (h_i + \zeta_i^n)$$

$$+ 8 u_j^{n+1/2} (h_i + \zeta_i^{n+1/2}) + 5 u_j^{n+1} (h_i + \zeta_i^{n+1})]$$

$$+ \frac{\Delta t}{24} (T_{kij} + P_{kij}) [-v_j^n (h_i + \zeta_i^n) + 8 v_j^{n+1/2} (h_i + \zeta_i^{n+1/2}) + 5 v_j^{n+1} (h_i + \zeta_i^{n+1})] \tag{A4}$$

$$\int\int_{\Omega^e} \frac{5}{24} \tau^{n+1} \nabla \cdot (W_k \mathbf{u}^{n+1}) R(\zeta^{n+1}) \,\mathrm{d}x\,\mathrm{d}y$$

$$= \frac{5}{24} \tau^{n+1} ((O_{kij} + U_{kij}) u_j^{n+1} + (P_{kij} + V_{kij}) v_j^{n+1}) \zeta_i^{n+1}$$

$$- \frac{5}{24} \tau^{n+1} ((O_{kij} + U_{kij}) u_j^{n+1} + (P_{kij} + V_{kij}) v_j^{n+1}) \zeta_i^{n+1/2}$$

$$- \frac{5\Delta t}{576} \tau^{n+1} \left( \begin{array}{l} ((C_{kijl} + Q_{kijl}) u_l^{n+1} + (E_{kijl} + S_{kijl}) v_l^{n+1}) [u_j^n (h_i + \zeta_i^n) + u_i^n (h_j + \zeta_j^n)] \\ + ((D_{kijl} + R_{kijl}) u_l^{n+1} + (F_{kijl} + T_{kijl}) v_l^{n+1}) [v_j^n (h_i + \zeta_i^n) + v_i^n (h_j + \zeta_j^n)] \end{array} \right)$$

$$+ \frac{5\Delta t}{72} \tau^{n+1} \left( \begin{array}{l} ((C_{kijl} + Q_{kijl}) u_l^{n+1} + (E_{kijl} + S_{kijl}) v_l^{n+1}) [u_j^{n+1/2} (h_i + \zeta_i^{n+1/2}) + u_i^{n+1/2} (h_j + \zeta_j^{n+1/2})] \\ + ((D_{kijl} + R_{kijl}) u_l^{n+1} + (F_{kijl} + T_{kijl}) v_l^{n+1}) [v_j^{n+1/2} (h_i + \zeta_i^{n+1/2}) + v_i^{n+1/2} (h_j + \zeta_j^{n+1/2})] \end{array} \right)$$

$$+ \frac{25\Delta t}{576} \tau^{n+1} \left( \begin{array}{l} ((C_{kijl} + Q_{kijl}) u_l^{n+1} + (E_{kijl} + S_{kijl}) v_l^{n+1}) [u_j^{n+1} (h_i + \zeta_i^{n+1}) + u_i^{n+1} (h_j + \zeta_j^{n+1})] \\ + ((D_{kijl} + R_{kijl}) u_l^{n+1} + (F_{kijl} + T_{kijl}) v_l^{n+1}) [v_j^{n+1} (h_i + \zeta_i^{n+1}) + v_i^{n+1} (h_j + \zeta_j^{n+1})] \end{array} \right) \tag{A5}$$

$$\int\int_{\Omega^e} \frac{5}{24} v_{\zeta^{n+1}} \nabla W_{k\perp} \cdot \nabla \zeta_{\perp}^{n+1} \,\mathrm{d}x\,\mathrm{d}y = \frac{5}{24} v_{\zeta^{n+1}} \left( J_{ki} + K_{ki} - \frac{1}{\|\mathbf{u}\|^2} ((Q_{kijl} u_l^{n+1} + R_{kijl} v_l^{n+1}) u_j^{n+1} \right.$$

$$\left. + (S_{kijl} u_l^{n+1} + T_{kijl} v_l^{n+1}) v_j^{n+1}) \right) \zeta_i^{n+1} \tag{A6}$$



DOI: 10.1002/fld

$$\int\int_{\Omega^e} W_k R(u^{n+1/2})\,\mathrm{d}x\,\mathrm{d}y$$
$$= M_{ki}(u_i^{n+1/2} - w_{xi}^{n+1/2}) - M_{ki}(u_i^n - w_{xi}^n) + \frac{\Delta t}{24} U_{ki}(5\zeta_i^n + 8\zeta_i^{n+1/2} - \zeta_i^{n+1})$$
$$+ \frac{\Delta t}{24} S_{kij}(5u_j^n u_i^n + 8u_j^{n+1/2} u_i^{n+1/2} - u_j^{n+1} u_i^{n+1})$$
$$+ \frac{\Delta t}{24} T_{kij}(5v_j^n u_i^n + 8v_j^{n+1/2} u_i^{n+1/2} - v_j^{n+1} u_i^{n+1}) \tag{A7}$$

$$\int\int_{\Omega^e} \frac{1}{3}\tau^{n+1/2} \nabla W_k \cdot \mathbf{u}^{n+1/2} R(u^{n+1/2})\,\mathrm{d}x\,\mathrm{d}y$$
$$= \frac{1}{3}\tau^{n+1/2}(U_{kij} u_j^{n+1/2} + V_{kij} v_j^{n+1/2})(u_i^{n+1/2} - w_{xi}^{n+1/2})$$
$$- \frac{1}{3}\tau^{n+1/2}(U_{kij} u_j^{n+1/2} + V_{kij} v_j^{n+1/2})(u_i^n - w_{xi}^n)$$
$$+ \frac{\Delta t}{72}\tau^{n+1/2}(J_{kij} u_j^{n+1/2} + X_{kij} v_j^{n+1/2})(5\zeta_i^n + 8\zeta_i^{n+1/2} - \zeta_i^{n+1})$$
$$+ \frac{\Delta t}{72}\tau^{n+1/2}(Q_{kijl} u_l^{n+1/2} + S_{kijl} v_l^{n+1/2})(5u_j^n u_i^n + 8u_j^{n+1/2} u_i^{n+1/2} - u_j^{n+1} u_i^{n+1})$$
$$+ \frac{\Delta t}{72}\tau^{n+1/2}(R_{kijl} u_l^{n+1/2} + T_{kijl} v_l^{n+1/2})(5v_j^n u_i^n + 8v_j^{n+1/2} u_i^{n+1/2} - v_j^{n+1} u_i^{n+1}) \tag{A8}$$

$$\int\int_{\Omega^e} \frac{1}{3} v_{u^{n+1/2}} \nabla W_{k\perp} \cdot \nabla u_\perp^{n+1/2}\,\mathrm{d}x\,\mathrm{d}y$$
$$= \frac{1}{3} v_{u^{n+1/2}} \left( J_{ki} + K_{ki} - \frac{1}{\|\mathbf{u}\|^2}((Q_{kijl} u_l^{n+1/2} + R_{kijl} v_l^{n+1/2}) u_j^{n+1/2} \right.$$
$$\left. + (S_{kijl} u_l^{n+1/2} + T_{kijl} v_l^{n+1/2}) v_j^{n+1/2}) \right) u_i^{n+1/2} \tag{A9}$$

$$\int\int_{\Omega^e} W_k R(u^{n+1})\,\mathrm{d}x\,\mathrm{d}y$$
$$= M_{ki}(u_i^{n+1} - w_{xi}^{n+1}) - M_{ki}(u_i^{n+1/2} - w_{xi}^{n+1/2}) + \frac{\Delta t}{24} U_{ki}(-\zeta_i^n + 8\zeta_i^{n+1/2} + 5\zeta_i^{n+1})$$
$$+ \frac{\Delta t}{24} S_{kij}(-u_j^n u_i^n + 8u_j^{n+1/2} u_i^{n+1/2} + 5u_j^{n+1} u_i^{n+1})$$
$$+ \frac{\Delta t}{24} T_{kij}(-v_j^n u_i^n + 8v_j^{n+1/2} u_i^{n+1/2} + 5v_j^{n+1} u_i^{n+1}) \tag{A10}$$



DOI: 10.1002/fld

$$\int\int_{\Omega^e} \frac{5}{24}\tau^{n+1}\nabla W_k \cdot \mathbf{u}^{n+1} R(u^{n+1})\,\mathrm{d}x\,\mathrm{d}y$$
$$= \frac{5}{24}\tau^{n+1}(U_{kij}u_j^{n+1} + V_{kij}v_j^{n+1})(u_i^{n+1} - w_{xi}^{n+1})$$
$$- \frac{5}{24}\tau^{n+1}(U_{kij}u_j^{n+1} + V_{kij}v_j^{n+1})(u_i^{n+1/2} - w_{xi}^{n+1/2})$$
$$+ \frac{5\Delta t}{576}\tau^{n+1}(J_{kij}u_j^{n+1} + X_{kij}v_j^{n+1})(-\zeta_i^n + 8\zeta_i^{n+1/2} + 5\zeta_i^{n+1})$$
$$+ \frac{5\Delta t}{576}\tau^{n+1}(Q_{kijl}u_l^{n+1} + S_{kijl}v_l^{n+1})(-u_j^n u_i^n + 8u_j^{n+1/2}u_i^{n+1/2} + 5u_j^{n+1}u_i^{n+1})$$
$$+ \frac{5\Delta t}{576}\tau^{n+1}(R_{kijl}u_l^{n+1} + T_{kijl}v_l^{n+1})(-v_j^n u_i^n + 8v_j^{n+1/2}u_i^{n+1/2} + 5v_j^{n+1}u_i^{n+1}) \quad \text{(A11)}$$

$$\int\int_{\Omega^e} \frac{5}{24} v_{u^{n+1}} \nabla W_{k\perp} \cdot \nabla u_\perp^{n+1}\,\mathrm{d}x\,\mathrm{d}y$$
$$= \frac{5}{24} v_{u^{n+1}} \left( J_{ki} + K_{ki} - \frac{1}{\|\mathbf{u}\|^2}((Q_{kijl}u_l^{n+1} + R_{kijl}v_l^{n+1})u_j^{n+1} + (S_{kijl}u_l^{n+1} + T_{kijl}v_l^{n+1})v_j^{n+1}) \right) u_i^{n+1} \quad \text{(A12)}$$

$$\int\int_{\Omega^e} W_k R(v^{n+1/2})\,\mathrm{d}x\,\mathrm{d}y$$
$$= M_{ki}(v_i^{n+1/2} - w_{y_i}^{n+1/2}) - M_{ki}(v_i^n - w_{y_i}^n) + \frac{\Delta t}{24}V_{ki}(5\zeta_i^n + 8\zeta_i^{n+1/2} - \zeta_i^{n+1})$$
$$+ \frac{\Delta t}{24}S_{kij}(5u_j^n v_i^n + 8u_j^{n+1/2}v_i^{n+1/2} - u_j^{n+1}v_i^{n+1})$$
$$+ \frac{\Delta t}{24}T_{kij}(5v_j^n v_i^n + 8v_j^{n+1/2}v_i^{n+1/2} - v_j^{n+1}v_i^{n+1}) \quad \text{(A13)}$$

$$\int\int_{\Omega^e} \frac{1}{3}\tau^{n+1/2}\nabla W_k \cdot \mathbf{u}^{n+1/2} R(v^{n+1/2})\,\mathrm{d}x\,\mathrm{d}y$$
$$= \frac{1}{3}\tau^{n+1/2}(U_{kij}u_j^{n+1/2} + V_{kij}v_j^{n+1/2})(v_i^{n+1/2} - w_{y_i}^{n+1/2})$$
$$- \frac{1}{3}\tau^{n+1/2}(U_{kij}u_j^{n+1/2} + V_{kij}v_j^{n+1/2})(v_i^n - w_{y_i}^n)$$
$$+ \frac{\Delta t}{72}\tau^{n+1/2}(K_{kij}u_j^{n+1/2} + Y_{kij}v_j^{n+1/2})(5\zeta_i^n + 8\zeta_i^{n+1/2} - \zeta_i^{n+1})$$



DOI: 10.1002/fld

$$+\frac{\Delta t}{72}\tau^{n+1/2}(Q_{kijl}u_l^{n+1/2}+S_{kijl}v_l^{n+1/2})(5u_j^n v_i^n+8u_j^{n+1/2}v_i^{n+1/2}-u_j^{n+1}v_i^{n+1})$$

$$+\frac{\Delta t}{72}\tau^{n+1/2}(R_{kijl}u_l^{n+1/2}+T_{kijl}v_l^{n+1/2})(5v_j^n v_i^n+8v_j^{n+1/2}v_i^{n+1/2}-v_j^{n+1}v_i^{n+1}) \quad \text{(A14)}$$

$$\int\int_{\Omega^e}\frac{1}{3}\nu_{v^{n+1/2}}\nabla W_{k\perp}\cdot\nabla v_\perp^{n+1/2}\,\mathrm{d}x\,\mathrm{d}y$$

$$=\frac{1}{3}\nu_{v^{n+1/2}}\left(J_{ki}+K_{ki}-\frac{1}{\|\mathbf{u}\|^2}((Q_{kijl}u_l^{n+1/2}+R_{kijl}v_l^{n+1/2})u_j^{n+1/2}\right.$$

$$\left.+(S_{kijl}u_l^{n+1/2}+T_{kijl}v_l^{n+1/2})v_j^{n+1/2})\right)v_i^{n+1/2} \quad \text{(A15)}$$

$$\int\int_{\Omega^e}W_k R(v^{n+1})\,\mathrm{d}x\,\mathrm{d}y$$

$$=M_{ki}(v_i^{n+1}-w_{y_i}^{n+1})-M_{ki}(v_i^{n+1/2}-w_{y_i}^{n+1/2})+\frac{\Delta t}{24}V_{ki}(-\zeta_i^n+8\zeta_i^{n+1/2}+5\zeta_i^{n+1})$$

$$+\frac{\Delta t}{24}S_{kij}(-u_j^n v_i^n+8u_j^{n+1/2}v_i^{n+1/2}+5u_j^{n+1}v_i^{n+1})$$

$$+\frac{\Delta t}{24}T_{kij}(-v_j^n v_i^n+8v_j^{n+1/2}v_i^{n+1/2}+5v_j^{n+1}v_i^{n+1}) \quad \text{(A16)}$$

$$\int\int_{\Omega^e}\frac{5}{24}\tau^{n+1}\nabla W_k\cdot\mathbf{u}^{n+1}R(v^{n+1})\,\mathrm{d}x\,\mathrm{d}y$$

$$=\frac{5}{24}\tau^{n+1}(U_{kij}u_j^{n+1}+V_{kij}v_j^{n+1})(v_i^{n+1}-w_{y_i}^{n+1})$$

$$-\frac{5}{24}\tau^{n+1}(U_{kij}u_j^{n+1}+V_{kij}v_j^{n+1})(v_i^{n+1/2}-w_{y_i}^{n+1/2})$$

$$+\frac{5\Delta t}{576}\tau^{n+1}(K_{kij}u_j^{n+1}+Y_{kij}v_j^{n+1})(-\zeta_i^n+8\zeta_i^{n+1/2}+5\zeta_i^{n+1})$$

$$+\frac{5\Delta t}{576}\tau^{n+1}(Q_{kijl}u_l^{n+1}+S_{kijl}v_l^{n+1})(-u_j^n v_i^n+8u_j^{n+1/2}v_i^{n+1/2}+5u_j^{n+1}v_i^{n+1})$$

$$+\frac{5\Delta t}{576}\tau^{n+1}(R_{kijl}u_l^{n+1}+T_{kijl}v_l^{n+1})(-v_j^n v_i^n+8v_j^{n+1/2}v_i^{n+1/2}+5v_j^{n+1}v_i^{n+1}) \quad \text{(A17)}$$



DOI: 10.1002/fld

$$\int\int_{\Omega^e} \frac{5}{24} v_{v^{n+1}} \nabla W_{k\perp} \cdot \nabla v_{\perp}^{n+1} \,\mathrm{d}x\,\mathrm{d}y$$
$$= \frac{5}{24} v_{v^{n+1}} \left( J_{ki} + K_{ki} - \frac{1}{\|\mathbf{u}\|^2} ((Q_{kijl} u_l^{n+1} + R_{kijl} v_l^{n+1}) u_j^{n+1} + (S_{kijl} u_l^{n+1} + T_{kijl} v_l^{n+1}) v_j^{n+1}) \right) v_i^{n+1} \tag{A18}$$

$$\int\int_{\Omega^e} W_k w_x \,\mathrm{d}x\,\mathrm{d}y = M_{ki} w_{x_i}$$
$$= -[\tfrac{1}{3}(Q_{kijl} u_i + R_{kijl} v_i) + \tfrac{1}{6}(C_{kijl} u_i + D_{kijl} v_i)] h_l h_j$$
$$-\tfrac{1}{2}[(Q_{kijl} u_j + R_{kijl} v_j) + (C_{kijl} u_j + D_{kijl} v_j)] h_l h_i \tag{A19}$$

$$\int\int_{\Omega^e} W_k w_y \,\mathrm{d}x\,\mathrm{d}y = M_{ki} w_{y_i}$$
$$= -[\tfrac{1}{3}(S_{kijl} u_i + T_{kijl} v_i) + \tfrac{1}{6}(E_{kijl} u_i + F_{kijl} v_i)] h_l h_j$$
$$-\tfrac{1}{2}[(S_{kijl} u_j + T_{kijl} v_j) + (E_{kijl} u_j + F_{kijl} v_j)] h_l h_i \tag{A20}$$

The definitions of coefficients appeared in Equations (A1)–(A20) are given below

$$B_k = \frac{\partial N_k}{\partial x}, \quad C_k = \frac{\partial N_k}{\partial y}, \quad J_{ki} = \int\int_{\Omega^e} \frac{\partial N_k}{\partial x} \frac{\partial N_i}{\partial x} \,\mathrm{d}x\,\mathrm{d}y, \quad K_{ki} = \int\int_{\Omega^e} \frac{\partial N_k}{\partial y} \frac{\partial N_i}{\partial y} \,\mathrm{d}x\,\mathrm{d}y$$

$$M_{ki} = \int\int_{\Omega^e} N_k N_i \,\mathrm{d}x\,\mathrm{d}y, \quad U_{ki} = \int\int_{\Omega^e} N_k \frac{\partial N_i}{\partial x} \,\mathrm{d}x\,\mathrm{d}y, \quad V_{ki} = \int\int_{\Omega^e} N_k \frac{\partial N_i}{\partial y} \,\mathrm{d}x\,\mathrm{d}y$$

$$J_{kij} = \int\int_{\Omega^e} N_j \frac{\partial N_k}{\partial x} \frac{\partial N_i}{\partial x} \,\mathrm{d}x\,\mathrm{d}y, \quad K_{kij} = \int\int_{\Omega^e} N_j \frac{\partial N_k}{\partial x} \frac{\partial N_i}{\partial y} \,\mathrm{d}x\,\mathrm{d}y$$

$$O_{kij} = \int\int_{\Omega^e} N_k \frac{\partial N_j}{\partial x} N_i \,\mathrm{d}x\,\mathrm{d}y, \quad P_{kij} = \int\int_{\Omega^e} N_k \frac{\partial N_j}{\partial y} N_i \,\mathrm{d}x\,\mathrm{d}y$$

$$S_{kij} = \int\int_{\Omega^e} N_k N_j \frac{\partial N_i}{\partial x} \,\mathrm{d}x\,\mathrm{d}y, \quad T_{kij} = \int\int_{\Omega^e} N_k N_j \frac{\partial N_i}{\partial y} \,\mathrm{d}x\,\mathrm{d}y$$

$$U_{kij} = \int\int_{\Omega^e} N_j \frac{\partial N_k}{\partial x} N_i \,\mathrm{d}x\,\mathrm{d}y, \quad V_{kij} = \int\int_{\Omega^e} N_j \frac{\partial N_k}{\partial y} N_i \,\mathrm{d}x\,\mathrm{d}y$$

$$X_{kij} = \int\int_{\Omega^e} N_j \frac{\partial N_k}{\partial y} \frac{\partial N_i}{\partial x} \,\mathrm{d}x\,\mathrm{d}y, \quad Y_{kij} = \int\int_{\Omega^e} N_j \frac{\partial N_k}{\partial y} \frac{\partial N_i}{\partial y} \,\mathrm{d}x\,\mathrm{d}y$$

$$C_{kijl} = \int\int_{\Omega^e} N_k \frac{\partial N_l}{\partial x} N_j \frac{\partial N_i}{\partial x} \,\mathrm{d}x\,\mathrm{d}y, \quad D_{kijl} = \int\int_{\Omega^e} N_k \frac{\partial N_l}{\partial x} N_j \frac{\partial N_i}{\partial y} \,\mathrm{d}x\,\mathrm{d}y$$



DOI: 10.1002/fld

$$E_{kijl}=\int\int_{\Omega^e} N_k \frac{\partial N_l}{\partial y} N_j \frac{\partial N_i}{\partial x}\,\mathrm{d}x\,\mathrm{d}y, \quad F_{kijl}=\int\int_{\Omega^e} N_k \frac{\partial N_l}{\partial y} N_j \frac{\partial N_i}{\partial y}\,\mathrm{d}x\,\mathrm{d}y$$

$$Q_{kijl}=\int\int_{\Omega^e} N_l \frac{\partial N_k}{\partial x} N_j \frac{\partial N_i}{\partial x}\,\mathrm{d}x\,\mathrm{d}y, \quad R_{kijl}=\int\int_{\Omega^e} N_l \frac{\partial N_k}{\partial x} N_j \frac{\partial N_i}{\partial y}\,\mathrm{d}x\,\mathrm{d}y$$

$$S_{kijl}=\int\int_{\Omega^e} N_l \frac{\partial N_k}{\partial y} N_j \frac{\partial N_i}{\partial x}\,\mathrm{d}x\,\mathrm{d}y, \quad T_{kijl}=\int\int_{\Omega^e} N_l \frac{\partial N_k}{\partial y} N_j \frac{\partial N_i}{\partial y}\,\mathrm{d}x\,\mathrm{d}y \tag{A21}$$

## REFERENCES


1. Peregrine DH. Long waves on a beach. *Journal of Fluid Mechanics* 1967; **27**:815–882.
2. Madsen PA, Murray R, Sørensen OR. A new form of the Boussinesq equations with improved linear dispersion characteristics. *Coastal Engineering* 1991; **15**(4):371–388.
3. Nwogu O. Alternative form of Boussinesq equations for near-shore wave propagation. *Journal of Waterway, Port, Coastal, and Ocean Engineering* (ASCE) 1993; **119**(6):618–638.
4. Wu TY. Nonlinear waves and solitons in water. *Physica D* 1998; **123**:48–63.
5. Abbott MB, McCowan AD, Warren IR. Accuracy of short wave numerical model. *Journal of Hydraulic Engineering* 1984; **110**(10):1287–1301.
6. Wei G, Kirby JT. A time-dependent numerical code for the extended Boussinesq equations. *Journal of Waterway, Port, Coastal, and Ocean Engineering* (ASCE) 1995; **121**(5):251–261.
7. Wang KH, Wu TY, Yates GT. Three dimensional scattering of solitary waves by vertical cylinder. *Journal of Waterway, Port, Coastal, and Ocean Engineering* (ASCE) 1992; **118**(5):551–566.
8. Li YS, Zhan JM. Boussinesq-type model with boundary-fitted coordinate system. *Journal of Waterway, Port, Coastal, and Ocean Engineering* (ASCE) 2001; **127**(3):152–160.
9. Shi F, Dalrymple RA, Kirby JT, Chen Q, Kennedy A. A fully nonlinear Boussinesq model in generalized curvilinear coordinates. *Coastal Engineering* 2001; **42**:337–358.
10. Katopodes ND, Wu C-T. Computation of finite-amplitude dispersive waves. *Journal of Waterway, Port, Coastal, and Ocean Engineering* (ASCE) 1987; **113**(4):327–346.
11. Antunes do Carmo JS, Seabra Santos FJ, Barthelemy E. Surface waves propagation in shallow water: a finite element model. *International Journal for Numerical Methods in Fluids* 1993; **16**:447–459.
12. Kawahara M, Cheng JY. Finite element method for Boussinesq wave analysis. *International Journal of Computational Fluid Dynamics* 1994; **2**:1–17.
13. Wu TY. Long waves in ocean and coastal waters. *Journal of Engineering Mechanics Division* (ASCE) 1981; **107**:501–522.
14. Langtangen HP, Pederson G. Computational models for weakly dispersive non-linear water waves. *Computer Methods in Applied Mechanics and Engineering* 1998; **160**:337–358.
15. Li YS, Liu S-X, Lai G-Z. Numerical modeling of boussinesq equations by finite element method. *Coastal Engineering* 1999; **37**:97–122.
16. Beji S, Nadaoka K. A formal derivation and numerical modeling of the improved Boussinesq equations for varying depth. *Ocean Engineering* 1996; **23**(8):691–704.
17. Walkley M, Berzins M. A finite element method for the one-dimensional extended Boussinesq equations. *International Journal for Numerical Methods in Fluids* 1999; **29**(2):143–157.
18. Walkley M, Berzins M. A finite element method for the two-dimensional extended Boussinesq equations. *International Journal for Numerical Methods in Fluids* 2002; **39**:865–885.
19. Woo S-B, Liu PL-F. Finite-element model for modified Boussinesq equations. I: model development. *Journal of Waterway, Port, Coastal, and Ocean Engineering* (ASCE) 2004; **130**(1):1–16.
20. Sørensen OR, Schäffer HA, Sørensen LS. Boussinesq-type modeling using an unstructured finite element technique. *Coastal Engineering* 2004; **50**:181–198.
21. Donea JR, Huerta A. *Finite Element Methods for Flow Problems*. Wiley: West Sussex, England, 2003.
22. Hughes TJR, Mallet M. A new finite element formulation for computational fluid dynamics. III. The generalized streamline operator for multidimensional advective–diffusive systems. *Computer Methods in Applied Mechanics and Engineering* 1986; **58**(3):305–328.




DOI: 10.1002/fld

23. Hughes TJR, Mallet M. A new finite element formulation for computational fluid dynamics. IV. A discontinuity-capturing operator for multidimensional advective–diffusive systems. *Computer Methods in Applied Mechanics and Engineering* 1986; **58**(3):329–336.
24. Codina R. A discontinuity-capturing crosswind-dissipation for the finite element solution of the convection-diffusion equation. *Computer Methods in Applied Mechanics and Engineering* 1993; **110**(3–4):325–342.
25. Isaacson M. Solitary wave diffraction around large cylinder. *Journal of Waterway*, *Port*, *Coastal*, *and Ocean Engineering* (ASCE) 1983; **109**(1):121–127.
26. Yates GT, Wang KH. Solitary wave scattering by a vertical cylinder: experimental study. *Proceedings of the Fourth* (*1994*) *International Offshore and Polar Engineering Conference*, Osaka, Japan, vol. 3, 1994; 118–124.
27. Wang KH, Jiang L. Solitary wave interactions with an array of two vertical cylinders. *Applied Ocean Research* 1994; **15**(6):337–350.
28. Ambrosi D, Quartapelle L. A Taylor–Galerkin method for simulating nonlinear dispersive water waves. *Journal of Computational Physics* 1998; **146**:546–569.
29. Donea JR, Huerta A. High-order accurate time-stepping schemes for convection–diffusion problems. *Computer Methods in Applied Mechanics and Engineering* 2000; **182**(3–4):249–275.
30. Donea JR. A Taylor–Galerkin method for convective transport problems. *International Journal for Numerical Methods in Engineering* 1984; **20**(1):101–119.
31. Hughes TJR, Franca LP, Hullbert GM. A new finite element formulation for computational fluid dynamics. VIII. The Galerkin/least-squares method for advective–diffusive equations. *Computer Methods in Applied Mechanics and Engineering* 1989; **73**(2):173–189.
32. Shakib F. Finite element analysis of the compressible Euler and Navier–Stokes Equations. *Ph.D. Thesis*, Stanford University, U.S.A., 1989.
33. Zhong Z. Time-accurate stabilized finite element model for nonlinear shallow water waves. *Ph.D. Thesis*, University of Houston, 2007.
34. Schember HR. A new model for three-dimensional nonlinear dispersive long waves. *Ph.D. Thesis*, California Institute of Technology, Pasadena, CA, 1982.
35. Teng MH, Wu TY. Nonlinear water waves in channels of arbitrary shape. *Journal of Fluid Mechanics* 1992; **242**:211–233.
36. Engelman MS, Sani JL, Gresho PM. The implementation of normal and/or tangential boundary condition in finite element codes for incompressible flow. *Internatioanl Journal for Numerical Methods in Fluids* 1982; **2**:225–238.
37. Power H, Chwang AT. On reflection of a planar solitary wave at a vertical wall. *Wave Motion* 1984; **6**:183–195.
38. Su CH, Mirie RM. On head-on collisions between two solitary waves. *Journal of Fluid Mechanics* 1980; **98**:509–525.
39. Yih CS, Wu TY. General solution for interaction of solitary waves including head-on collisions. *Acta Mechanica Sinica* 1995; **11**(3):193–199.
40. Mirie RM, Su CH. Collisions between two solitary waves. Part 2. A numerical study. *Journal of Fluid Mechanics* 1982; **115**:475–492.
41. Li YA, Hyman JM, Choi W. A numerical study of the exact evolution equations for surface waves in water of finite depth. *Studies in Applied Mathematics* 2004; **113**:303–324.



DOI: 10.1002/fld